AD-A286 578

||||||||||||||||||||||||

Experimental and Theoretical Evaluation of Elastic Waves in Curved Layered Media
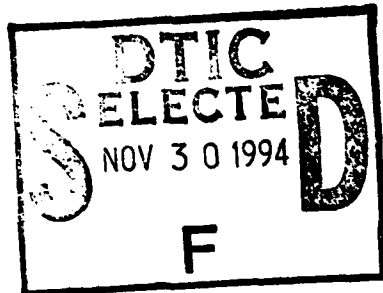
TECHNICAL – THIRD INTERIM

Report Period: 1 Oct 1992 – 31 May 1994

Date: July 1994

Prepared under Contract No N61533-91-K-0032

for

Naval Surface Warfare Center
(Carderock Division)

Dale E. Chimenti
Ali Safaeinilli

Center For Nondestructive Evaluation
Iowa State University
Ames, IA 50010

Leo B. Felsen
Smaine Zeroug[1]

Department of Electrical and Computer Engineering
Polytechnic Institute of New York
Brooklyn NY 11201

---

[1] Present address: Schlumberger-Doll Research
Old Quarry Road
Ridgefield, CT 06877-4108

94-35468

||||||||||||||||||||||||

DTIC QUALITY INSPECTED 5

This document has been approved
for public release and sale; its
distribution is unlimited.

94 11 16 086

Abstract

This report describes the progress achieved during the third period of the study of elastic wave reflection from the curved and planar media subject to water loading. During the previous period, extensive experimental investigations were initiated to study parametrically the behavior of acoustic beams at curved and planar fluid-solid interfaces. Three types of materials, representative of Navy applications, in two geometries and two sizes, and many values of incident angle and angular or linear coordinates were included in the effort of last year. Simultaneously, an aggressive program of theoretical modeling and experimental verification were mounted and essentially all of the data were compared to predictions of the model. We found, in most cases, very good agreement between model calculations and experimental data. For the theoretical modeling of these effects, the complex source point (CSP) method was used to produce Gaussian line sources to account for the wave-solid interaction for acoustic beams. The scattering problem solved in this work is couched in terms of spectral integrals that are approximated by high-frequency uniform asymptotics. The resulting expressions for the reflected field contain interacting specularly reflected beam and leaky wave contributions which establish the physical basis for the observed phenomena. In addition to the two-dimensional modeling for comparison to experiments, work began to formulate a 3-D beam model within the theoretical framework for this more complicated circumstance as well. In continuation of the efforts of last year, we have extended the two-dimensional model to three dimensions. Furthermore, we have extended our measurement capabilities from a CW data acquisition system to time-domain pulse excitation system. The new measurement scheme has provided us with a wealth of information that has lead to uncovering "whispering gallery" modes in solid curved structures; these had not been previously isolated in the CW measurements. All of the measurements in this report are obtained using a time-domain acquisition system. The calculations and measurements in this report have been concentrated on cylindrical shells with a variety of material parameters and dimensions.

Contents

ii

List of Tables

List of Figures

iv

Acknowledgments .

Overview

The objective of this program is to improve nondestructive inspection of curved layered structures by ultrasonic modeling and experiments on waves in fluid-loaded plates. We are accomplishing this by performing experimental and theoretical studies of the interaction of bounded transducer beams with curved layered solids. Our approach is a systematic one, in which we build progressively to a high level of understanding of scattering and reflection in the complicated materials under study in this project.

Nondestructive inspection of plate- or shell-like structures plays a critical role in Navy applications. Many components of naval systems are fabricated in plate or shell geometries. Ultrasonic testing of such structures effectively allows detection or sizing of internal discontinuities or sampling of material properties. Typical of this class of fleet inspection problems is the case of RAM coatings bonded to metal superstructure. In the corrosive hot/wet/saline environment these coatings are subject to disbonding at the metal-polymer interface. Prior work on plate waves excited by beams in purely planar fluid-solid (FS) geometries has demonstrated the sensitivity of this type of ultrasonic wave mode to subtle internal defects [1, 2]. The extension of the analysis and measurements to curved plates and acoustically lossy media will permit us to achieve the full discrimination potential of the method in realistic structures of interest to the Navy.

The contract milestones established for this reporting period (1 Oct 1992 to 30 July 1994) are:

MILESTONES – FY 93/94

93-1 Continue measurements and comparisons with prediction of beam algorithm

93-2 Iterate model calculation and/or experimental procedure, as necessary based on comparisons

93-3 Generalize Gaussian beam model to curved fluid-loaded plates; extend algorithm to analyze re-radiated fields for this geometry

1

In the body of this report the accomplishments achieved in this work to date are described in detail. To highlight these items of progress we list them here in summary form for quick reference.

ACCOMPLISHMENTS – FY 93

- Additional measurements and comparisons carried out for solid cylindrical geometry **1**

- Model calculation improved based on experimental results; reflected field was modeled with complex receiver point **2**

- Commercial transducer beam was modeled using complex Gaussian functions Gaussian beam model was extended to include cylindrical shells **2**

- Experiments were carried out for cylindrical shells (several materials and radii) using commercial transducers and results were compared to model calculation with good agreement **3**

- Whispering gallery modes were observed in the solid cylinder experiment and verified using a ray model ★

- Data acquisition was carried out in the time-domain (pulse excitation) using a precision multi-axis scanner ★

- Time/frequency characteristics of the received signal are available for analysis ★

- Extended CSP Gaussian beam model from 2-D to a 3-D formulation ★

Notes: Bold numbers key to FY93 milestones; ★ denotes unplanned additional progress.

1 Introduction

In this report we present the recent theoretical and experimental progress in our work on the study of acoustic wave behavior in the interaction between ultrasonic beams and cylindrical shell structures. In the previous report period, we concentrated on theoretical and experimental results obtained for both flat plates and solid cylindrical structures. The problem of nonspecular reflection of bounded beam from solid structures has been extensively studied over the past 40 years, but in particular in the last 20 years [3, 4]. Essentially all of these efforts have been cn planar solids, both halfspaces and plates. Other studies on reflection of sound from cylinders [5, 6] has concentrated on effectively planar incident fields, where the sound wave field does not vary appreciably over the cylinder diameter.

Our problem, nonspecular sound beam reflection from cylindrical shells, draws on experience gained and knowledge developed in these related studies but differs significantly in that our incident field has a substantial spatial variation on the scale of the cylinder radius. Zeroug and Felsen [7, 8] studied theoretically the non-specular reflection of a divergent incident beam from planar interface and collimated beam from curved interface. In the analysis, plane interface results were extended to the more general conditions of a curved interface and the divergent incident beam field. By the Complex-Source-Point (CSP) method, which places a radiation source at a complex coordinate location, a conventional line or point source excited field can be converted into a two or three-dimensional quasi-Gaussian beam field which is an exact solution of the dynamical equations. When the CSP field interacts with a plane or cylindrically layered elastic medium, the resulting internal and external fields can be expressed rigorously in terms of wavenumber spectral integrals. Asymptotic reduction of these integrals, achieved by the steepest descent method applied to deformed contours in the complex spectral wavenumber plane, accounts for all relevant wave phenomena. For the reflected field, this yields explicit waveforms which are synthesized by interacting the specularly reflected beam, leaky wave, and possible lateral wave contribution. Comparison to the extensive experimental results of Zhang, et al. [9] and Chimenti, et al. [10] for these geometries has shown very good agreement with the predictions of approximate calculations based on the procedure outlined above.

This report will present our experimental and theoretical studies of the non-specular reflection of collimated acoustic beams generated by a commercially available piston radiator upon fluid-loaded cylindrical shells with air or fluid internal loading. In Section 2, we present an extension of the 2-D CSP model to 3 dimensions. Although for the case of reflection of the acoustic wave from a cylinder, a 2-D model is sufficient, the 3-D model gives us the capability of modeling wave reflection from more complicated objects. Also it can provide us with a more realistic picture of the experiment. In Section 3, the theory of the complex source point is extended to a complex receiver point and with the use of the reciprocity theorem, the voltage induced in the receiving transducer can be calculated very efficiently. In the experimental front, we have extended our capabilities from CW mode measurements to both CW and time-domain pulsed mode. The time-domain data is obtained using a new and very reliable equipment that is available to us at the Center for NDE at Iowa State University. A description of this system and experimental procedure is discussed in Section 4. In Section 5, the results of the experiments are discussed. These results include the detection of "Whispering Gallery" modes in the solid cylinder and other experiments on cylindrical shells. The experiments on the cylindrical shells were carried out for a variety of radii and materials. Finally a summary of the report and plans for outyear research are presented in Section 6.

4

2   Theory

During the previous period, a 2-D CSP model was developed to provide theoretical result for comparison with the experimental measurements. Although for most experiments done over cylindrical structures a 2-D model is sufficient, a 3-D model has been developed to provide capability to model wave reflection from more complicated objects. In the following section, the 3-D CSP model is described for both flat plate and cylindrical structures.

2.1   Flat plate structures

As is customary in the application of the CSP technique, we first consider scattering of the pressure field P in the fluid excited by a high-frequency real line or point source in the presence of a plane stratified structure comprised of homogeneous fluid and isotropic solid layers. The geometry is shown in Figure 1. With the source located at $\underline{r}'$, the time-harmonic pressure P at an observation point $\underline{r}$ in the fluid can be derived from a displacement potential field $\Phi(\underline{r};\underline{r}')$,

$$P(\underline{r};\underline{r}') = -\rho_f \omega^2 \Phi(\underline{r};\underline{r}') \quad \text{for } \underline{r} \neq \underline{r}', \tag{1}$$

where ρ_f is the fluid density, ω is the angular frequency and a time dependence $\exp(-i\omega t)$ is assumed and suppressed. The potential field in the fluid satisfies the source-excited Helmholtz equation

$$(\nabla^2 + k_f^2)\Phi(\underline{r};\underline{r}') = -\delta(\underline{r} - \underline{r}'), \qquad k_f = \omega/v_f \tag{2}$$

subject to a radiation condition at infinity, and with boundary conditions that account for the layers. In the above, v_f is the sound speed in the fluid. We find the solution by expressing the potential $\Phi(\underline{r};\underline{r}')$ in terms of an infinite spectrum of plane waves via spectral decompositions along the space coordinates tangential to the layer boundaries [11].

2.1.1   3-D fields

For three-dimensional fields, excited by a point source, $\underline{r}' \equiv (x',y',z')$, $\underline{r} \equiv (x,y,z)$, and $\delta(\underline{r} - \underline{r}') = \delta(x - x')\delta(y - y')\delta(z - z')$. We employ the plane

5
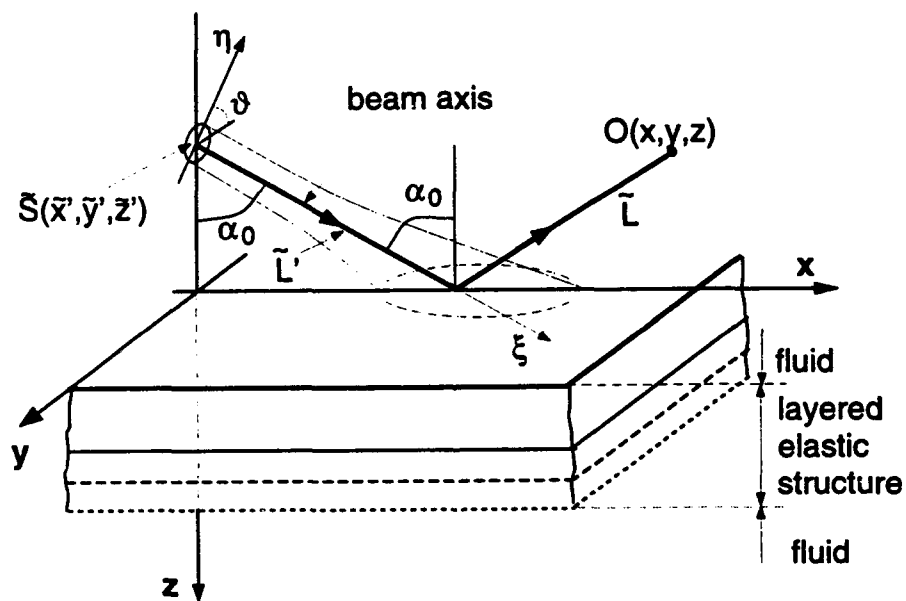
Figure 1: Flate plate geometry

wave spectral decomposition,

$$\Phi_{3D}(\underline{r};\underline{r}') = \frac{1}{(2\pi)^2} \int_{-\infty}^{\infty} \int_{-\infty}^{\infty} \hat{\Phi}_{3D}(k_x, k_y) \exp[ik_x(x - x') + ik_y(y - y')]dk_x dk_y.$$

(3)

Upon substitution of Eq. (3) into Eq. (2), one obtains the reduced wave equation for the spectral amplitude $\hat{\Phi}_{3D}(k_x, k_y)$, which (for point source excitation) is solved to yield.

$$\hat{\Phi}_{3D}(k_x, k_y) = \frac{i}{2\kappa_f} \left\{ \exp[i\kappa_f|z - z'|] + R(k_x, k_y) \exp\left[-i\kappa_f(z + z')\right] \right\}, \quad z \le 0$$

(4)

where κ_f is defined as,

$$\kappa_f = \sqrt{k_f^2 - (k_x^2 + k_y^2)}, \quad \text{Im}\{\kappa_f\} \ge 0$$

(5)

In Eq. (4), the spectral domain reflection coefficient $R(k_x, k_y)$, which takes into account the layered environment in $z \ge 0$, is evaluated by assuming plane wave incidence from the fluid and enforcing the well known boundary conditions at the fluid-solid interface at $z = 0$ and at subsequent solid-solid and solid-fluid interfaces for $z > 0$. Due to isotropy along the (x, y) plane. $R(k_x, k_y)$ is always expressed in terms of the total transverse wavenumber $k^2 = (k_x^2 + k_y^2)$, as is κ_f in Eq. (5). Therefore, it is convenient to perform the change of variables to the angular spectrum

$$k_x = k \cos\gamma, \quad k_y = k \sin\gamma, \quad dk_x dk_y = k \, dk \, d\gamma.$$

(6)

The spectral solution in Eq. (4) for the field in the fluid region excited by a real source can be converted via the CSP technique [12]-[13] into the solution due to a beam input by displacing the source point into the complex plane via analytic continuation

$$
\begin{aligned}
x' \rightarrow \tilde{x}' &= x' + ib\sin\alpha_0, \\
y' \rightarrow \tilde{y}' &= y', \\
z' \rightarrow \tilde{z}' &= z' + ib\cos\alpha_0
\end{aligned}
$$

(7)

where a tilde denotes a complex coordinate as well as functions of a complex coordinate, and

$$b \text{ real } > 0,$$

$$-\pi \le \alpha_0 \le +\pi.$$

(8)

The real-space field radiated by this complex source is a rotationally symmetric 3D beam with a quasi-Gaussian amplitude whose maximum lies along the angular direction α_0 contained in the plane (x, z). Its waist is centered at $(\underline{r}')$ and its $1/e$ width w_0 is specified by the real parameter b through $w_0 = \sqrt{2b/k_f}$, which establishes b as the Fresnel length of the beam. Insertion of Eq. (4) into Eq. (3), and use of Eqs. (6)-(8) yields the angular spectral integral representation of the total beam-excited field in the fluid, which can be written as the sum of an incident and reflected part,

$$\tilde{\Phi}_{3D}(\underline{r}; \tilde{\underline{r}}') = \tilde{\Phi}_{3D}^i(\underline{r}; \tilde{\underline{r}}') + \tilde{\Phi}_{3D}^r(\underline{r}; \tilde{\underline{r}}'), \tag{9}$$

where

$$\tilde{\Phi}_{3D}^i(\underline{r}; \tilde{\underline{r}}') = \frac{i}{8\pi^2} \int_{-\pi}^{+\pi} \int_0^{+\infty} \frac{k \exp[i\tilde{P}_{3D}^i(k, \gamma)]}{\sqrt{k_f^2 - k^2}} dk \, d\gamma, \tag{10}$$

and

$$\tilde{\Phi}_{3D}^r(\underline{r}; \tilde{\underline{r}}') = \frac{i}{8\pi^2} \int_{-\pi}^{+\pi} \int_0^{+\infty} \frac{k R(k) \exp[i\tilde{P}_{3D}^r(k, \gamma)]}{\sqrt{k_f^2 - k^2}} dk \, d\gamma \tag{11}$$

with

$$\tilde{P}_{3D}^{i,r}(k, \gamma) = k \cos \gamma \, (x - \tilde{x}') + k \sin \gamma \, (y - \tilde{y}') \pm \sqrt{k_f^2 - k^2} \, (z \mp \tilde{z}'). \tag{12}$$

In Eq. (12), the upper and lower signs pertain to the incident field $\tilde{\Phi}_{3D}^i(\underline{r}; \tilde{\underline{r}}')$ and reflected field $\tilde{\Phi}_{3D}^r(\underline{r}; \tilde{\underline{r}}')$, respectively.

2.1.2   2-D fields

For two-dimensional fields excited by a uniform line source parallel to the y-axis, one has $\underline{r}' \equiv (x', z')$, $\underline{r} \equiv (x, z)$, $\delta(\underline{r}-\underline{r}') \equiv \delta(x-x')\delta(z-z')$, with $\partial/\partial y \equiv 0$. Spectral decomposition along x of the displacement potential satisfying the two-dimensional form of the wave equation (2) leads to a solution of the spectral amplitudes as in Eq. (4) but with $k_y \equiv 0$. The conversion from the real line source field to a two-dimensional sheet beam field is accomplished through the relations in Eq. (7), with omission of the second equation. The final spectral integral representation for the total sheet-beam-excited field can then be written similarly to Eq. (9) as in Eqs. (9)-(11),

$$\tilde{\Phi}_{2D}(\underline{r}; \tilde{\underline{r}}') = \tilde{\Phi}_{2D}^i(\underline{r}; \tilde{\underline{r}}') + \tilde{\Phi}_{2D}^r(\underline{r}; \tilde{\underline{r}}'), \tag{13}$$

where

$$\tilde{\Phi}^i_{2D}(\underline{r};\tilde{\underline{r}}') = \frac{i}{4\pi} \int_{-\infty}^{+\infty} \frac{\exp[i\tilde{P}^i_{2D}(k_x)]}{\sqrt{k_f^2 - k_x^2}} dk_x \qquad (14)$$

and

$$\tilde{\Phi}^r_{2D}(\tilde{\underline{r}};\underline{r}') = \frac{i}{4\pi} \int_{-\infty}^{+\infty} \frac{R(k_x)\exp[i\tilde{P}^r_{2D}(k_x)]}{\sqrt{k_f^2 - k_x^2}} dk_x \qquad (15)$$

with

$$\tilde{P}^{i,r}_{2D}(k_x) = k_x(x - \tilde{x}') \pm \sqrt{k_f^2 - k_x^2}\,(z \mp \tilde{z}'). \qquad (16)$$

2.1.3 Asymptotic solutions

When evaluated numerically, the exact solutions in Eqs. (10-16) furnish reference data for the field everywhere. For beam waist locations more than a few wavelengths away from the layer interface, the spectral integrals can be reduced asymptotically by the saddle point method applied to single and double integrals in the complex k_x and (k, γ) planes, respectively, as developed in [11]. Asymptotic evaluation furnishes explicit results with physical interpretations that highlight the relevant wave phenomena. In the following, we summarize the final resulting asymptotic expressions. A detailed account of the asymptotic procedure can be found in [14]-[15].

2.1.4 3D complex ray field

The three dimensional incident field can be expressed as

$$\tilde{\Phi}^i_{3D}(\underline{r};\tilde{\underline{r}}') = \frac{\exp[ik_f\tilde{L}_i]}{4\pi\tilde{L}_i}, \qquad (17)$$

where

$$\tilde{L}_i \equiv \sqrt{(x - \tilde{x}')^2 + (y - \tilde{y}')^2 + (z - \tilde{z}')^2}, \quad \text{Re}\{\tilde{L}_i\} \geq 0. \qquad (18)$$

The three dimensional nonspecular reflected field may be expressed as

$$\tilde{\Phi}^r(\underline{r},\tilde{\underline{r}}') \sim R(\tilde{k}_{sr})\frac{\exp[ik_f(\tilde{L}' + \tilde{L})]}{4\pi(\tilde{L}' + \tilde{L})}$$

9

$$- \frac{\exp[-i\pi/4]}{2\sqrt{2\pi}} \sum_{j=1}^{M} \frac{\mathrm{Res}\{R(k)\}_{k_{p_j}}}{\sqrt{\tilde{\rho}}} \sqrt{\frac{k_{p_j}}{k_j^2 - k_{p_j}^2}} \exp[i\tilde{P}_{3D}^r(k_{p_j}, \tilde{\gamma}_{sr})] \tau(-i\tilde{s}_{p_j}) \quad (19)$$

where,

$$\check{L}' = -\tilde{z}'/\cos\tilde{\theta}_{sr}, \quad \check{L} = -z/\cos\tilde{\theta}_{sr}, \quad (20)$$

$$\tilde{\rho} = \sqrt{(x - \tilde{x}')^2 + (y - \tilde{y}')^2}, \quad \mathrm{Re}[\tilde{\rho}] \geq 0, \quad (21)$$

The first term in Eq. (19) corresponds to the saddle point contribution and describes the specularly reflected field. The second term in Eq. (19) corresponds to residue contributions from M simple pole singularities that are assumed to be near the saddle point. The uniform asymptotic expression for the saddle point contribution can be obtained by applying the transition function $\tau()$. The transition function $\tau()$ can be expressed as

$$\tau(-i\tilde{s}_p) = -\frac{\exp[-(-i\tilde{s}_p)^2]}{2\sqrt{\pi}(-\tilde{s}_p)} + \frac{1}{2}\mathrm{erfc}(-i\tilde{s}_p), \quad (22)$$

$$\tilde{s}_p = \sqrt{i\left[P(\zeta_s) - P(\zeta_p)\right]}, \zeta_{s,p} = \left\{ \begin{array}{ll} (k_{s,p}, \gamma_s) & 3D \\ (k_{xs,xp}) & 2D \end{array} \right\}.$$

Here erfc in Eq. (22) is the complementary error function defined by

$$\mathrm{erfc}(q) = \frac{2}{\sqrt{\pi}} \int_q^\infty \exp[-t^2]dt. \quad (23)$$

whereas the "numerical distance" $\tilde{s}_{p_j}$ corresponding to the pole k_{p_j} is,

$$\tilde{s}_{p_j} = \sqrt{i\left[\tilde{P}_{3D}^r(\tilde{k}_{sr}, \tilde{\gamma}_{sr}) - \tilde{P}_{3D}^r(k_{p_j}, \tilde{\gamma}_{sr})\right]}. \quad (24)$$

2.1.5   2D complex ray field

The two-dimensional incident field can be expressed as

$$\tilde{\Phi}_{2D}^i(\underline{r}; \tilde{\underline{r}}') \sim \frac{\exp[i\pi/4]}{2\sqrt{2\pi}} \frac{\exp[ik_f\tilde{l}_i]}{\sqrt{k_f\tilde{l}_i}}, \quad (25)$$

10

with

$$\tilde{l}_i \equiv \sqrt{(x - \tilde{x}')^2 + (z - \tilde{z}')^2}, \quad \text{Re}\{\tilde{l}_i\} \geq 0. \qquad (26)$$

The two-dimensional nonspecular reflected field can be expressed as

$$\tilde{\Phi}^r_{2D}(\underline{r}; \tilde{\underline{r}}') \sim R(\tilde{k}_s) \frac{\exp[i\pi/4]}{2\sqrt{2\pi}} \frac{\exp[ik_f(\tilde{l}' + \tilde{l})]}{\sqrt{k_f(\tilde{l}' + \tilde{l})}}$$

$$-\frac{1}{2} \sum_{j=1}^{M} \frac{\text{Res}\{R(k)\}_{k_{p_j}}}{\sqrt{k_f^2 - k_{p_j}^2}} \exp[i\tilde{P}^r_{2D}(k_{p_j})]\tau(-i\tilde{s}_{p_j}), \qquad (27)$$

where

$$\tilde{l}' = -\tilde{z}'/\cos\tilde{\theta}_{xs}, \quad \tilde{l} = -\tilde{z}/\cos\tilde{\theta}_{xs}, \qquad (28)$$

and $\tilde{\theta}_{xs}$ is the complex angle corresponding to the saddle point $\tilde{k}_{xs} = k_f \sin \tilde{\theta}_{xs}$ for the 2D reflected field. Moreover, $\tilde{s}_{p_j}$ now becomes

$$\tilde{s}_{p_j} = \sqrt{i\left[\tilde{P}^r_{2D}(\tilde{k}_{xs}) - \tilde{P}^r_{2D}(k_{p_j})\right]}, \qquad (29)$$

2.2 Cylindrical structures

As in the case of the flat plate, we begin with the pressure field P in the fluid excited by a time-harmonic high-frequency line or point source located at $\underline{r}'$ in the presence of an elastic structure composed of homogeneous isotropic cylindrical layers. The pressure at an observation point $\underline{r}$ can be derived from a displacement potential field $\Phi(\underline{r}; \underline{r}')$ which satisfies the wave equation Eq.(2) subject to a radiation condition at infinity and appropriate boundary conditions at the outermost interface of radius a. The 3-D boundary value problem is solved in the spectral wavenumber domain corresponding to the (ϕ, z) coordinates perpendicular to the stratification; for 2-D, the z-dependence is omitted. The azimuthal domain is extended from its physical $-\pi \leq \phi \leq \pi$ range to an infinite domain $-\infty \leq \phi \leq \infty$ in order to remove the 2π- periodicity constraint from the traveling azimuthal wave spectra [16, 17], [11]. The periodicity in the physical angular domain $-\pi \leq \phi \leq \pi$, which leads to standing wave solutions, can be restored by placing in the unbounded ϕ domain an infinite array of image sources but this shall not be required here.

11

2.2.1 3-D fields

Referring to the defining equation for the potential Φ in Eq.(1) and to the wave equation Eq.(2), we have the cylindrical coordinate representations,

$$\nabla^2 \equiv \frac{1}{\rho}\frac{\partial}{\partial\rho}\rho\frac{\partial}{\partial\rho} + \frac{1}{\rho^2}\frac{\partial^2}{\partial\phi^2} + \frac{\partial^2}{\partial z^2} \tag{30}$$

$$\delta(\underline{r} - \underline{r}') = \frac{\delta(\rho - \rho')}{\rho'}\delta(\phi - \phi')\delta(z - z') \tag{31}$$

with $\underline{r}' \equiv (\rho', \phi', z')$ being the real source point location, and $\underline{r} \equiv (\rho, \phi, z)$. Then, the spectral representation of the real-source-point $\Phi(\underline{r}; \underline{r}')$ can be written as,

$$\Phi_{3D}(\underline{r}; \underline{r}') = \frac{1}{(2\pi)^2}\int_{-\infty}^{\infty} d\nu \int_{-\infty}^{\infty} d\beta \hat{\Phi}_{3D}(\nu, \beta)\exp[i\nu(\phi - \phi') + i\beta(z - z')]. \tag{32}$$

A time dependence $\exp(-i\omega t)$ is suppressed. In Eq. (32), $\hat{\Phi}_{3D}(\nu, \beta)$ is the 3D spectral amplitude defined by the reduced (radial) wave equation,

$$\left[\frac{d}{d\rho}\rho\frac{d}{d\rho} + \frac{1}{\rho}(\kappa_f^2\rho^2 - \nu^2)\right]\hat{\Phi}_{3D}(\nu, \beta) = -\delta(\rho - \rho') \tag{33}$$

The solution of Eq. (33) involves Bessel and Hankel functions. By a formulation that emphasizes inward $(-\rho)$ and outward $(+\rho)$ traveling waves as expressed by the Hankel function $H_\nu^{(2)}$ and $H_\nu^{(1)}$, respectively, one finds [16, 17]

$$\hat{\Phi}_{3D}(\nu, \beta) = \frac{i\pi}{4}\left[H_\nu^{(2)}(\kappa_f\rho_<) + R(\nu, \beta)\frac{H_\nu^{(2)}(\kappa_f a)}{H_\nu^{(1)}(\kappa_f a)}H_\nu^{(1)}(\kappa_f\rho_<)\right]H_\nu^{(1)}(\kappa_f\rho_>), \tag{34}$$

where ρ and rho' are larger than a. In Eq. (34), $\rho_>$ and $\rho_<$ denote the larger and lesser of ρ and ρ', respectively, while $R(\nu, \beta)$ is the spectral domain reflection coefficient at the fluid-solid interface $\rho = a$. Insertion of Eq. (34) into Eq. (32) yields the spectral integral representation of the total field in the fluid excited by a point source at a real location. To convert these results to

12

beam-type fields, we perform the following CSP substitution on the cartesian coordinates of the real source,

$$
\begin{aligned}
x' \to \tilde{x}' &= x' + ib\cos\alpha_z \sin\alpha_\phi, \\
y' \to \tilde{x}' &= y' + ib\cos\alpha_z \cos\alpha_\phi, \\
z' \to \tilde{z}' &= z' + ib\sin\alpha_z
\end{aligned} \tag{35}
$$

with

$$
b \text{ real } > 0; \quad -\pi \le (\alpha_\phi, \alpha_z) \le +\pi. \tag{36}
$$

As in [14], the tilde ˜ denotes a complex quantity. The CSP in cylindrical coordinates follows from the familiar relations [18, 19],

$$
\begin{aligned}
\rho' \to \tilde{\rho}' &= \sqrt{\tilde{x}'^2 + \tilde{y}'^2}, \quad \mathrm{Re}\{\tilde{\rho}'\} \ge 0, \\
\phi' \to \tilde{\phi}' &= \tan^{-1}\left[\tilde{x}'/\tilde{y}'\right], \quad \text{with} \quad \tilde{\phi}' = \pi \quad \text{when} \quad \tilde{x}' = 0.
\end{aligned} \tag{37}
$$

The formulation in Eq. (34), with Eqs. (35)-(37), while useful for analyzing the scattered asymptotic field, is indirect for extraction of the incident beam field which travels from the source to the observer without encountering the cylinder. In fact, the incident beam field is contributed in part by the first term in the spectral amplitude in Eq. (34), and in part by a portion of the second term. The complication, arising from the cylindrical coordinate representation and discussed previously shall be avoided here entirely by inserting for the incident beam field $\tilde{\Phi}^i_{3L}$ its known coordinate-invariant free-space form, which describes in real space a rotationally symmetric 3D beam with quasi-Gaussian amplitude profile; the beam maximum (beam axis) is along the direction specified by the angle α_z with respect to the (x, y) plane and by the angle α_ϕ with respect to the y axis in the (x, y) plane. Anticipating the asymptotic evaluation, the analytically continued total beam-excited field in the fluid can then be written as

$$
\tilde{\Phi}_{3D}(\underline{r}; \tilde{\underline{r}}') = \tilde{\Phi}^i_{3D}(\underline{r}; \tilde{\underline{r}}') + \tilde{\Phi}^r_{3D}(\underline{r}; \tilde{\underline{r}}'), \tag{38}
$$

where the scattered field $\tilde{\Phi}^r_{3D}(\underline{r}; \tilde{\underline{r}}')$ is given asymptotically by

$$
\begin{aligned}
\tilde{\Phi}^r_{3D}(\underline{r}; \tilde{\underline{r}}') \sim{} & \frac{i}{16\pi} \int d\nu \int_{-\infty}^{\infty} d\beta \, R(\nu, \beta) \frac{H^{(2)}_\nu(\kappa_f a)}{H^{(1)}_\nu(\kappa_f a)} H^{(1)}_\nu(\kappa_f \tilde{\rho}') H^{(1)}_\nu(\kappa_f \rho) \\
& \exp[i\nu(\phi - \tilde{\phi}') + i\beta(z - \tilde{z}')],
\end{aligned} \tag{39}
$$

13

Omission of the $\nu-$integration limits in Eq. (39) signifies that we shall utilize only that portion of the ν angular spectrum which establishes the scattered field and does not contribute to the incident field. For asymptotic evaluation of the integral in Eq. (39), the Hankel functions in the integrand are approximated by Debye asymptotic forms that are valid in the parametric regimes of interest here [11],

$$H_\nu^{(1,2)}(\tau) \sim \sqrt{\frac{2}{\pi \tau \sin \gamma}} \exp[\mp i\pi/4] \exp\left[\pm i\tau \sin\gamma \mp i\nu\gamma\right] \qquad (40)$$

with the following definitions and restrictions,

$$\cos\gamma = \frac{\nu}{\tau}, \quad 0 < \mathrm{Re}\gamma < \pi, |\arg\{\tau\}| < \pi/2, |\nu| < |\tau|, |\nu - \tau| > O(|\nu|^{1/3}). \qquad (41)$$

For the relevant ν spectral interval that yields the scattered field, the following conditions apply,

$$|\nu| < (|\kappa_f \rho|, |\kappa_f \tilde{\rho}'|, |\kappa_f a|)$$
$$|\nu - (|\kappa_f \rho|, |\kappa_f \tilde{\rho}'|, |\kappa_f a|)| > O(|\nu|^{1/3})$$
$$\rho, \tilde{\rho}', a \gg \kappa_f^{-1}. \qquad (42)$$

This yields

$$\check{\Phi}_{3D}^r(\underline{r}; \underline{\tilde{r}}') \sim \frac{i}{8\pi^2 \sqrt{\rho\tilde{\rho}'}} \int d\nu \int_{-\infty}^{\infty} d\beta R(\nu,\beta) \frac{\exp\left[i\check{P}_{3D}^r(\nu,\beta)\right]}{\kappa_f \sqrt{\sin\gamma \sin\tilde{\gamma}'}} \qquad (43)$$

with

$$\check{P}_{3D}^r(\nu,\beta) = \kappa_f \left[\rho\sin\gamma + \tilde{\rho}'\sin\tilde{\gamma}' - 2a\sin\gamma_a\right] - \nu\left[\gamma + \tilde{\gamma}' - 2\gamma_a - (\phi - \tilde{\phi}')\right] + \beta(z - \tilde{z}'). \qquad (44)$$

Here, γ, $\tilde{\gamma}'$, and γ_a are defined by

$$\gamma = \cos^{-1}\frac{\nu}{\kappa_f \rho}, \quad \tilde{\gamma}' = \cos^{-1}\frac{\nu}{\kappa_f \tilde{\rho}'}, \quad \gamma_a = \cos^{-1}\frac{\nu}{\kappa_f a}. \qquad (45)$$

According to the second condition in Eq. (41), the angles in Eq. (45) are restricted to $0 < \mathrm{Re}\{\gamma, \tilde{\gamma}', \gamma_a\} < \pi$.

14

2.2.2 2-D fields

For 2-D excitation, the source distribution is assumed uniform along the axial direction. This eliminates the z-coordinate from the problem, leaving a spectral decomposition of the total field in the azimuthal direction only. Accordingly, $\beta \equiv 0$ in the radial wave equation (Eq. (33)) and the solution in Eq. (34), thereby reducing $\kappa_f \equiv k_f$. The CSP substitutions for the 2-D sheet beam incident normally with respect to the axial direction then yield Eq. (37), with $\alpha_z = 0$. The total field in the fluid due to the 2-D CSP beam source is written as

$$\tilde{\Phi}_{2D}(\underline{r};\tilde{\underline{r}}') = \tilde{\Phi}^i_{2D}(\underline{r};\tilde{\underline{r}}') + \tilde{\Phi}^r_{2D}(\underline{r};\tilde{\underline{r}}'). \tag{46}$$

The asymptotically approximated incident beam field $\tilde{\Phi}^i_{2D}(\underline{r};\tilde{\underline{r}}')$ will subsequently be written down directly in its known coordinate invariant form, whereas the asymptotic scattered field is expressed by the approximate spectral integral

$$\tilde{\Phi}^r_{2D}(\underline{r};\tilde{\underline{r}}') \sim \frac{i}{4\pi k_f \sqrt{\rho\tilde{\rho}'}} \int d\nu \, R(\nu) \, \frac{\exp\left[i\tilde{P}^r_{2D}(\nu)\right]}{\sqrt{\sin\gamma\sin\tilde{\gamma}'}} \tag{47}$$

with

$$\tilde{P}^r_{2D}(\nu) = k_f \left[\rho\sin\gamma + \tilde{\rho}'\sin\tilde{\gamma}' - 2a\sin\gamma_a\right] - \nu\left[\gamma + \tilde{\gamma}' - 2\gamma_a - (\phi - \tilde{\phi}')\right]. \tag{48}$$

The angles γ, $\tilde{\gamma}'$, and γ_a are defined in Eq. (45) with $\kappa_f \to k_f$.

2.2.3 Asymptotic solutions

Since the forms of the integrals in Eq. (43) and Eq. (47) are similar to the integrals dealt with in the planar geometry [14], we can employ the same generic procedure detailed for the flat plate to perform the asymptotic evaluation here. Thus, we shall approximate each integral by the contributions arising from the saddle point and the pole singularities of the spectral reflection coefficient in a uniform manner which accounts for the proximity of these critical points. Despite similarities between the integrals in the planar and cylindrical formulations, there are fundamental differences in the wave

15

phenomena in these two geometries due to differences in the complex phase functions. Furthermore, unlike its plane wave counterpart, the cylindrical wave reflection coefficient $R(\nu, \beta)$ depends on both spectral variables. This fact leads to a more complex evaluation procedure and correspondingly more complex wave behavior in the cylindrical geometry. For clarity, we treat the simpler 2-D case first.

2.2.4 2-D Asymptotic nonspecular reflected fields

Asymptotic evaluation of the integral in Eq. (47) by the saddle point method requires determination of the saddle point(s) $\tilde{\nu}_s$ in the phase function $\tilde{P}_{2D}^r(\nu)$ of the integrand. Setting the ν-derivative of $\tilde{P}_{2D}^r$ equal to zero yields implicitly,

$$\cos^{-1}\left[\frac{\tilde{\nu}_s}{k_f\rho}\right] + \cos^{-1}\left[\frac{\tilde{\nu}_s}{k_f\tilde{\rho}'}\right] - 2\cos^{-1}\left[\frac{\tilde{\nu}_s}{k_f a}\right] = (\phi - \tilde{\phi}'). \tag{49}$$

The contribution from the saddle point (denoted by $\tilde{\Phi}_{2D,sp}^r(\underline{r};\underline{\tilde{r}}')$) along the steepest descent path (SDP) can then be expressed in ray-based coordinates as follows ([11], Sec.6.7)

$$\tilde{\Phi}_{2D,sp}^r(\underline{r};\underline{\tilde{r}}') \sim R(\tilde{\nu}_s)\frac{\exp[ik_f(\tilde{l}'+\tilde{l})+i\pi/4]}{2\sqrt{2\pi k_f(\tilde{l}'+\tilde{l})}}\sqrt{\left.\frac{a(\tilde{l}'+\tilde{l})\sin\gamma_a}{2\tilde{l}'\tilde{l}+a(\tilde{l}'+\tilde{l})\sin\gamma_a}\right|_{\tilde{\nu}_s}}, \tag{50}$$

where the complex lengths $\tilde{l}'$ and $\tilde{l}$, respectively, are extensions of the distances from the beam waist center to the interface and from the interface to the observer, measured along the specularly reflected path segment. They are defined by,

$$\tilde{l}' = \tilde{\rho}'\sin\tilde{\gamma}' - a\sin\gamma_a|_{\tilde{\nu}_s}, \quad \tilde{l} = \rho\sin\gamma - a\sin\gamma_a|_{\tilde{\nu}_s}. \tag{51}$$

The expression in Eq. (50) describes the high-frequency quasi-Gaussian beam field reflected from a cylindrically curved surface with radius a, and characterized by a slowly varying reflection coefficient $R(\nu)$. Such a reflected complex ray field can be constructed directly via complex ray theory without the spectral synthesis employed here [18, 19]. One notes in particular that the last term in Eq. (50), expressed by the square root, determines primarily the

effect of the surface curvature on the reflected beam. This term, which approaches unity as the radius of curvature becomes very large, is the analytic extension of the divergence factor well known in (real) ray theory.

In addition to the saddle point contribution (specular reflection) in Eq. (50), we must account for contributions from spectral poles of $R(\nu)$ crossed during the deformation of the integration contour into the SDP. We are interested especially in the regime where $R(\nu)$ is not slowly varying but possesses pole singularities near the saddle point. This requires uniform asymptotics as detailed [14]. The uniform asymptotic reduction of the scattered field integral in Eq. (47) thus becomes

$$\check{\Phi}^r_{2D}(\rho, \check{\rho}') \sim \check{\Phi}^r_{2D,sp}(\underline{r}; \underline{\check{r}}') - \frac{1}{2} \sum_{j=1}^{M} \frac{\mathrm{Res}\{R(\nu)\}_{\nu_{p_j}}}{k_f \sqrt{\rho\rho' \sin \check{\gamma} \sin \check{\gamma}'}|_{\nu_{p_j}}} \exp[i\check{P}^r_{2D}(\nu_{p_j})]\tau(-i\check{s}_{p_j})$$

(52)

with $\check{\Phi}^r_{2D,sp}(\underline{r}; \underline{\check{r}}')$ given in Eq. (50), the phase $\check{P}^r_{2D}$ given in Eq. (48), $\check{l}$ and $\check{l}'$ in Eq. (51), the angles γ, $\check{\gamma}'$, and γ_a in Eq. (45) with $\kappa_f \rightarrow k_f$, and the saddle point $\check{\nu}_s$ defined by the relation in Eq. (49). The numerical distance $\check{s}_{p_j}$ is defined by

$$\check{s}_{p_j} = \sqrt{i[\check{P}^r_{2D}(\check{\nu}_s) - \check{P}^r_{2D}(\nu_{p_j})]} \; ; \qquad \arg\left[\check{s}_{p_j}\right] = \arg\left[\nu_{p_j} - \check{\nu}_s\right] - \arg\left[\mathrm{SDP}|_{\check{\nu}_s}\right]$$

(53)

where $\arg\left[\mathrm{SDP}|_{\check{\nu}_s}\right]$ represents the argument of $d\nu$ along the SDP at $\nu = \check{\nu}_s$ and ν_{p_j} represents the jth pole of the reflection coefficient $R(\nu)$, with residue denoted by $\mathrm{Res}\{R(\nu)\}_{\nu_{p_j}}$. The first term in Eq. (52) identifies the specularly reflected beam field in Eq. (50). The second term in Eq. (52) comprises residue contributions from M simple pole singularities that are assumed to be near the saddle point, and it describes the contributing leaky waves made uniform by the transition function $\tau()$ given in Eq. 22. As for the planar case, the form of the transition function in Eq. 22 is retained intact to yield a robust and versatile algorithm for beams incident at arbitrary angles and with arbitrary collimations (see Sec.3.2.2 in [14]). Because of curvature-induced beam divergence, in contrast to planar geometry [1], both diverging and well collimated incident beams give rise to broad excursions of the reflected field saddle point $\check{\nu}_s$ in the complex ν-plane. This behavior, which is associated

17

only with diverging beams in the planar geometry, leads to saddle point proximities near most of the relevant leaky wave poles, thereby requiring use of the full expression for τ, whereas that expression could have been approximated asymptotically for various parameter ranges in the planar case (see [14]). The validity of the asymptotic solution in Eq. (52) will be checked against the reference solution obtained by direct numerical integration of the spectral integral in Eq. (47).

2.2.5   3-D Asymptotic nonspecular reflected fields

As mentioned earlier, the asymptotic reduction for this case requires careful handling since the reflection coefficient $R(\nu, \beta)$ depends on both spectral wavenumbers. This fact will become clear when evaluating the residue contribution of a pole singularity of $R(\nu, \beta)$. First, let us evaluate the saddle point contribution, assuming a slowly varying $R(\nu, \beta)$. First, the saddle point $(\tilde{\nu}_s, \tilde{\beta}_s)$ of the phase $\tilde{P}^r_{3D}(\nu, \beta)$ in Eq. (44) is found to satisfy the following simultaneous equations,

$$\left[\gamma + \tilde{\gamma}' - 2\gamma_a - (\phi - \tilde{\phi}')\right]_{\tilde{\nu}_s, \tilde{\beta}_s} = 0$$

$$\left[\beta\left[k_f^2 - \beta^2\right]^{-1/2}(\rho \sin\gamma + \tilde{\rho}' \sin\tilde{\gamma}' - 2a \sin\gamma_a)\right]_{\tilde{\nu}_s, \tilde{\beta}_s} - (z - \tilde{z}') = 0 \quad (54)$$

where the angles γ, $\tilde{\gamma}'$, and γ_a are defined in Eq. (45). The complex geometrical lengths $\tilde{l}'$ and $\tilde{l}$ are defined by

$$\tilde{l}' = \tilde{\rho}' \sin\tilde{\gamma}' - a \sin\gamma_a|_{\tilde{\nu}_s, \tilde{\beta}_s}; \quad \tilde{l} = \rho \sin\gamma - a \sin\gamma_a|_{\tilde{\nu}_s, \tilde{\beta}_s}, \quad (55)$$

and we introduce the more convenient angular wavenumber variable ϑ defined by

$$\beta = k_f \sin\vartheta, \quad \kappa_f = k_f \cos\vartheta. \quad (56)$$

Using Eqs. (55) and (56), it is possible to evaluate the phase at the saddle point $(\tilde{\nu}_s, \tilde{\beta}_s)$ or $(\tilde{\nu}_s, \tilde{\vartheta}_s)$ and write it in the following form,

$$\tilde{P}^r_{3D}(\tilde{\nu}_s, \tilde{\vartheta}_s) = k_f\left[(\tilde{l}' + \tilde{l})\cos\vartheta + (z - \tilde{z}')\sin\vartheta\right]_{\tilde{\nu}_s, \tilde{\vartheta}_s} = k_f\left[\tilde{L}' + \tilde{L}\right]_{\tilde{\nu}_s, \tilde{\vartheta}_s} \quad (57)$$

where $\tilde{L}'$ and $\tilde{L}$ are shown in Figure 1(a).   The resulting saddle point
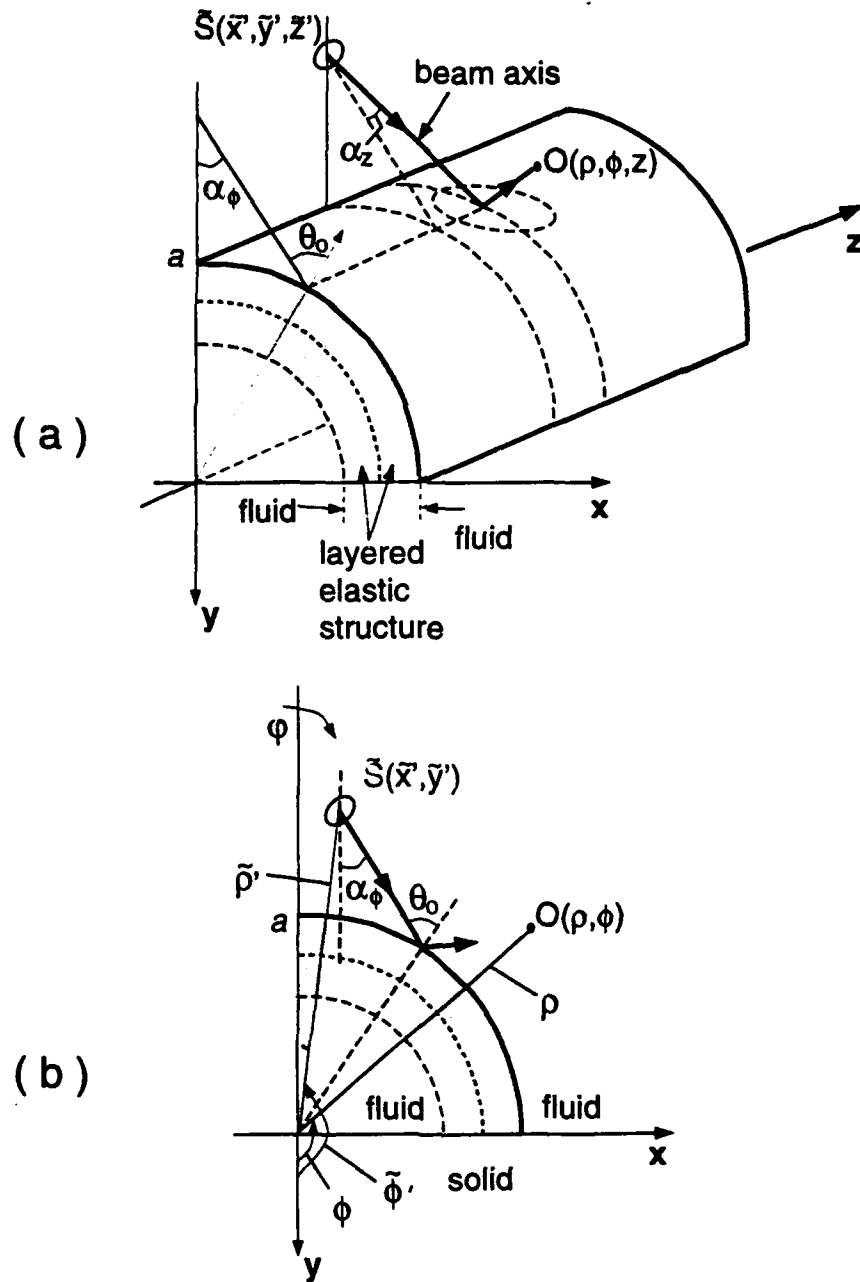
Figure 2: The geometry of the cylindrical configuration for a 3D CSP beam incident on a cylindrical surface.

contribution can be written in the following complex ray form,

$$\tilde{\Phi}^r_{3D,sp}(\underline{r},\underline{r}') \sim R(\tilde{\nu}_s, \tilde{\beta}_s)\frac{\exp\left[ik_f(\hat{L}' + \hat{L})\right]}{4\pi(\hat{L}' + \hat{L})}\sqrt{\frac{a(\tilde{l}' + \tilde{l})\sin\gamma_a}{2\tilde{l}'\tilde{l} + a(\tilde{l}' + \tilde{l})\sin\gamma_a}}|_{\tilde{\nu}_s, \tilde{\beta}_s}, \quad (58)$$

where all quantities are evaluated at $(\tilde{\nu}_s, \tilde{\beta}_s)$. This expression represents the 3D quasi-Gaussian beam reflected from a cylindrical surface under specular conditions where $R(\nu, \beta)$ is slowly varying in the vicinity of $(\tilde{\nu}_s, \tilde{\beta}_s)$. In particular, the square root in Eq. (58) can be interpreted as the divergence coefficient which contains the effect of the interface curvature on the 3D CSP beam. We note that this complex ray field can also be constructed directly via a CSP-extended ray theory ([11], Sec.6.7).

We turn now to the residue contributions. Let $R(\nu, \beta)$ be given by,

$$R(\nu, \beta) = N(\nu, \beta)\left[D(\nu, \beta)\right]^{-1} \quad (59)$$

Pole singularities of $R(\nu, \beta)$ satisfy

$$D(\nu, \beta) = 0 \quad (60)$$

which defines a dispersion relation for the guided modes of the structure that can be solved formally as

$$\nu_p \equiv \nu_p(\beta) \quad \text{or} \quad \beta_p \equiv \beta_p(\nu). \quad (61)$$

The subscript "p" refers to a pole singularity. Assuming that the ν integration is performed first, the residue contribution of the intercepted pole $\nu_p(\beta)$ in the ν plane is followed by integration along the SDP in the β plane which passes by the saddle point $\tilde{\beta}'_s$ of the phase $i\tilde{P}^r_{3D}[\nu_p(\beta), \beta]$ defined as (the prime on $\tilde{\beta}'_s$ distinguishes this quantity from $\tilde{\beta}_s$ defined in Eq. (54)),

$$\frac{d\tilde{P}^r_{3D}\left[\nu_p(\tilde{\beta}'_s), \tilde{\beta}'_s\right]}{d\beta} \equiv \left[\frac{\partial\tilde{P}^r_{3D}}{\partial\beta} + \frac{\partial\tilde{P}^r_{3D}}{\partial\nu}\frac{\partial\nu_p(\beta)}{\partial\beta}\right]_{\nu_p(\tilde{\beta}'_s), \tilde{\beta}'_s} = 0 \quad (62)$$

Using the explicit expressions of the partial derivatives of the phase in Eq. (44), we can write the condition in Eq. (62) in the following form

$$\Delta\tilde{z}_2 = a\Delta\tilde{\phi}_2\left[-\frac{d\nu_p(\beta)/a}{d\beta}\right]_{\nu_p(\tilde{\beta}'_s), \tilde{\beta}'_s} \quad (63)$$

20

where (see Figure 1(b))

$$\Delta \tilde{z}_2 = \left[-\beta [k_f^2 - \beta^2]^{-1/2} (\rho \sin \gamma + \tilde{\rho}' \sin \tilde{\gamma}' - 2a \sin \gamma_a) \right]_{\nu_p(\tilde{\beta}_s'), \tilde{\beta}_s'} + (z - \tilde{z}')$$

$$\Delta \tilde{\phi}_2 = - \left[\gamma + \tilde{\gamma}' - 2\gamma_a - (\phi - \tilde{\phi}') \right]_{\nu_p(\tilde{\beta}_s'), \tilde{\beta}_s'}. \tag{64}$$

The asymptotic expression for the residue contribution in the ν plane, followed by saddle point evaluation in the β plane, can be written as,

$$\tilde{\Phi}_{3D,res}^r(\underline{r}, \underline{\tilde{r}}') \sim -\frac{1}{4\pi} \sum_{j=1}^{M} \frac{N(\tilde{p}_j)}{\partial D(\tilde{p}_j)/\partial \nu} \frac{\epsilon(\tilde{p}_j) \exp \left[i \tilde{P}_{3D}^r(\tilde{p}_j) \right]}{\sqrt{(k_f^2 - \beta^2) \rho \tilde{\rho}' \sin \gamma \sin \tilde{\gamma}' |_{\tilde{p}_j}}} \sqrt{\frac{2\pi i}{d^2 \tilde{P}_{3D}^r(\tilde{p}_j)/d\beta^2}}, \tag{65}$$

where $\tilde{p}_j \equiv \left[\nu_{p_j}(\tilde{\beta}_s'), \tilde{\beta}_s' \right]$, with $\nu_{p_j}(\tilde{\beta}_s')$ and $\tilde{\beta}_s'$ computed from the simultaneous solution of Eqs. (60) and (62), respectively. We shall refer to this expression as the nonuniform LW field. The quantity $\epsilon(\tilde{p}_j)$ is defined generically by

$$\epsilon(k_p) = \begin{cases} 1, & \text{if SDP intercepts } k_p \\ 1/2, & \text{if SDP passes through } k_p \\ 0, & \text{otherwise.} \end{cases} \tag{66}$$

Furthermore, in Eq. (65)

$$d^2 \tilde{P}_{3D}^r(\tilde{p}_j)/d\beta^2 \equiv \left\{ \tilde{P}_{3D,\nu\nu}^r \left[d\nu_p(\beta)/d\beta \right]^2 + 2 \tilde{P}_{3D,\nu\beta}^r \left[d\nu_p(\beta)/d\beta \right] \right.$$
$$\left. + \tilde{P}_{3D,\nu}^r \left[d^2 \nu_p(\beta)/d\beta^2 \right] + \tilde{P}_{3D,\beta\beta}^r \right\}_{\tilde{p}_j}, \tag{67}$$

where the comma denotes partial differentiation with respect to the indicated variable, i.e. $\tilde{P}_{3D,\nu}^r \equiv \partial \tilde{P}_{3D}^r / \partial \nu$ and $\tilde{P}_{3D,\nu\beta}^r \equiv \partial^2 \tilde{P}_{3D}^r / \partial \nu \partial \beta$, etc.. The derivatives $d\nu_p(\beta)/d\beta$ and $d^2 \nu_p(\beta)/d\beta^2$ can be defined from implicit differentiation of the dispersion relation (60) as follows [20]

$$\frac{d\nu_p(\beta)}{d\beta}|_{\tilde{p}} = -\frac{D_{,\beta}}{D_{,\nu}}|_{\tilde{p}} \tag{68}$$

$$\frac{d^2 \nu_p(\beta)}{d\beta^2}|_{\tilde{p}} = -\frac{(D_{,\beta})^2 D_{,\nu\nu} - 2 D_{,\nu} D_{,\beta} D_{,\nu\beta} + (D_{,\nu})^2 D_{,\beta\beta}}{(D_{,\nu})^3}|_{\tilde{p}}. \tag{69}$$

21

The phase function of the nonuniform leaky wave field in Eq. (65) can be interpreted in terms of geometrical paths as follows (see Figure 1(b))

$$i\tilde{P}_{3D}^r\left[\nu_p(\tilde{\beta}_s'), \tilde{\beta}_s'\right] = ik_f(\tilde{L}_1 + \tilde{L}_3) + i\tilde{\beta}_s'\Delta\tilde{z}_2 + i\nu_p\Delta\tilde{\phi}_2, \qquad (70)$$

where the complex lengths $\Delta\tilde{z}_2$ and $\Delta\tilde{\phi}_2$ have been defined in Eq. (64) and are identified, respectively, as the projections onto the z and azimuthal ϕ directions of the LW path on the cylindrical surface. The complex lengths $\tilde{L}_1$ and $\tilde{L}_3$, shown in Figure 1(b), are defined by

$$\tilde{L}_1 = \frac{\tilde{\rho}'\sin\tilde{\gamma}' - a\sin\gamma_a}{\cos\tilde{\vartheta}'_s}\Big|_{\nu_p(\tilde{\beta}_s'),\tilde{\beta}_s'} \quad ; \quad \tilde{L}_3 = \frac{\rho\sin\gamma - a\sin\gamma_a}{\cos\tilde{\vartheta}'_s}\Big|_{\nu_p(\tilde{\beta}_s'),\tilde{\beta}_s'}, \quad (71)$$

where $\tilde{\vartheta}'_s$ is related to $\tilde{\beta}_s'$ through the transformation in Eq. (56).

It should be noted that we can also obtain the nonuniform residue contribution by performing the β integration first, picking up the residue at $\beta_p = \beta_p(\nu)$ followed by saddle point evaluation of the integral in the ν plane. The equivalence of the two results can be established by noting that

$$\frac{d^2\tilde{P}_{3D}^r\left[\nu_p(\tilde{\beta}_s'), \tilde{\beta}_s'\right]}{d\beta^2} \equiv \frac{d^2\tilde{P}_{3D}^r\left[\beta_p(\tilde{\nu}_s'), \tilde{\nu}_s'\right]}{d\nu^2}\left[\frac{d\beta_p(\nu)}{d\nu}\right]^{-2} \quad \text{and}$$

$$\frac{d\beta_p(\nu)}{d\nu} \equiv \left[\frac{d\nu_p(\beta)}{d\beta}\right]^{-1} \qquad (72)$$

where the last equality in Eq. (72) can be derived from Eq. (68), and its counterpart obtained by considering $\beta \equiv \beta(\nu)$.

To obtain the uniform asymptotic expression representing the nonspecular reflected field, we multiply the residue contributions $\tilde{\Phi}_{3D,res}^r(\underline{r},\underline{\tilde{r}}')$ by the transition function $\tau(-i\tilde{s}_{p_j})$ and add to the result the specular reflected field $\tilde{\Phi}_{3D,sp}^r(\underline{r},\underline{\tilde{r}}')$ to obtain,

$$\tilde{\Phi}_{3D}^r(\underline{r},\underline{\tilde{r}}') = \tilde{\Phi}_{3D,sp}^r(\underline{r},\underline{\tilde{r}}') + \tilde{\Phi}_{3D,res}^r(\underline{r},\underline{\tilde{r}}')\tau(-i\tilde{s}_{p_j}), \qquad (73)$$

where $\tilde{\Phi}^r_{3D,sp}(\underline{r}, \underline{\tilde{r}'})$ is given by Eq. (58), and $\tilde{\Phi}^r_{3D,res}(\underline{r}, \underline{\tilde{r}'})$ is given by Eq. (65) with $\epsilon(\tilde{p}_j) = 1$, $j = 1, M$. The numerical distance accounting for the proximity of the saddle point and the jth pole is defined by

$$
\tilde{s_{p_j}} = \sqrt{i \left[\tilde{P}^r_{3D}(\tilde{\nu}_s, \tilde{\beta}_s) - \tilde{P}^r_{3D}\left(\tilde{\nu}_{p_j}(\tilde{\beta}'_s), \tilde{\beta}'_s \right) \right]},
$$
$$
\arg\{\tilde{s_{p_j}}\} = \arg\{\nu_{p_j}(\tilde{\beta}'_s) - \tilde{\nu}_s\} - \arg\{\mathrm{SDP}|_{\tilde{\nu}_s}\}. \tag{74}
$$

2.3 Complex Receiver Point

The idea of the complex source point can be extended to the receiving transducer. The reciprocity theorem can be used efficiently to calculate the voltage in the receiving transducer. The idea of the complex receiver point transducer follows directly from that of complex source point. The reciprocal transducer which can both radiate and receive will be called the complex transducer point (CTP). The voltage E_R received by a transducer can be expressed as a convolution of the impinging field, due to source $\mathcal{S}$, with the receiving transfer function of $\mathcal{R}$. E_R can be written as

$$E_R = \frac{Z_L}{Z_L + H_{00}} \int \int H_{01}(k_x, k_y) N_S(k_x, k_y) dk_x \, dk_y, \qquad (75)$$

where $H_{01}(k_x, k_y)$ is the spectral receiving characteristic of transducer $\mathcal{R}$ and $N_S(k_x, k_y)$ is the spectral amplitude of plane waves emanating from $\mathcal{S}$. H_{00} is the electrical impedance of the receiver with no plane wave incident and Z_L is the load impedance of the receiver circuit. The contours of integration in Eq. (75) are taken along the real axis in the k_x and k_y planes. Since transducer $\mathcal{R}$ is reciprocal, the receiving characteristic H_{01} can be expressed in terms of its radiating characteristic H_{10}

$$H_{01}(k_x, k_y) = \frac{2\gamma}{\omega\rho} H_{10}(-k_x, -k_y), \quad \gamma = \sqrt{k_f^2 - k_x^2 - k_y^2}, \qquad (76)$$

where ρ is the fluid density. $H_{10}(k_x, k_y)$ can in turn be related to the spectral amplitude $O_R(k_x, k_y)$ of the pressure field radiated by $\mathcal{R}$ when it is energized by a current I_R through the relation $O_R(k_x, k_y) = H_{10}(k_x, k_y) I_R$. Finally, the induced voltage E_R can be written as

$$E_R = \frac{2K}{\omega\rho} \int \int [\gamma O_R(-k_x, -k_y) O_S(k_x, k_y) e^{i\gamma(z-z')} e^{i[k_x(x-x')+k_y(y-y')]} dk_X \, dk_y, \qquad (77)$$

where $K = Z_L/[I_R(Z_L + H_{00})]$ is a frequency-dependent factor that can be measured experimentally. In Eq. (77), the primed and unprimed coordinates refer to the aperture centers $\mathcal{S}$ and $\mathcal{R}$, respectively. Taking $P(k_x, k_y)$ and $V_z(k_x, k_y)$ as the spectral amplitudes of the pressure field $p(r, r')$ and axial z velocity $v_z(r, r')$ radiated by either transducer, defined in terms of two-dimensional Fourier transform as

$$P(k_x, k_y) = (\frac{1}{2\pi})^2 \int \int p(x, y, z) e^{-i(k_x + k_y)} dx dy \qquad (78)$$

24

and

$$V(k_x, k_y) = (\frac{1}{2\pi})^2 \int\int v(x,y,z)e^{-i(k_x x+k_y y)}dx dy \qquad (79)$$

then $O_{R,S}$ are related to $P(k_x, k_y)$ and $V_z(k_x, k_y)$ through the relations

$$\{P_{R,S}(k_x, k_y), V_{z(R,S)}(k_x, k_y)\} = \{1, \eta\}O_{R,S}(k_x, k_y)e^{i(\gamma(z-z'))}, \quad \eta = \frac{\gamma}{\rho\omega}. \quad (80)$$

In Eq. (78), the integral over (x, y) is performed in a plane of constant z.

It can be shown that voltage E_R within the paraxial approximation can be written as

$$E_R = K' \int\int [p_S(x,y,z;X,Y)\exp\{-\frac{X^2+Y^2}{w^2(Re\{z_R\})}\}\exp\{ik\frac{X^2+Y^2}{2c(Re\{z_R\})}\}]dX\,dY, \qquad (81)$$

where $w(z)$ is the $1/e$ width at z and $c(z)$ is the on axis radius of the curvature defined as

$$c(z) = z + b^2/z, \qquad w(z) = w_0\sqrt{1+\frac{z^2}{b^2}}, \qquad w_0 = \sqrt{\frac{2b}{k}}. \qquad (82)$$

In our case, where the source and the receiver points are located in the complex plane, the received voltage E_R can be written as

$$E_R = -i\pi\omega\rho K V_R V_S \frac{e^{iKR}}{4\pi R}, \qquad (83)$$

where

$$R = \sqrt{(x+x_R-x'-x_S)^2 + (y+y_R-y'-y_S)^2 + (z+z_R-z'-z_S)^2}. \qquad (84)$$

The case where the radiating CSP is located at $(0,0,0)$ and the axis is lying along z and the receiving CRP, whose waist is at (x,y,z) and axis lies in a direction α_R in the xz plane, results in

$$R = \sqrt{(x - ib_R\sin\alpha_R)^2 + y^2 + (z - ib_R\cos\alpha_R)^2}, \qquad (85)$$

where b_S and b_R determine the $1/e$ widths of the source and the receiver, i.e. $w_S = \sqrt{2b_S/k}$ and $w_R = \sqrt{2b_R/k}$. The paraxial approximation yields

$$R \sim z - iB_z + \frac{(x-iB_x)^2 + y^2}{2(z - iB_z)}, B_x = b_R\sin\alpha_R B_z = b_R\cos\alpha_R. \qquad (86)$$

25

Finally, the expression for E_R can be written as .

$$E_R \sim \frac{-i\pi\omega\rho K V_R V_S}{4\pi(z - iB_z)} \exp\{ik[z + \frac{(x - x_1)^2 + y^2}{2C(z)}] - \frac{(x - x_2)^2 + y^2}{W^2(z)} - \frac{ikB_x^2}{2z}\},$$
$$(87)$$

where $C(z)$ is the on axis radius of curvature of the received beam wavefront, $W(z)$ is its $1/e$ width at z, $x_1 = B_x B_z / z$ is the x-coordinate of the paraxial wavefront center of curvature, and $x_2 = B_x z / B_z$ is the line of maximum amplitude of the received beam field.

3 Experimental Procedure

During this reporting period, the experiments have concentrated on characterizing cylindrical shells. These experiments involve measuring the reflected field from a curved fluid-solid interface. The samples, equipment, and testing procedures are described below.

3.1 Sample preparation

Cylindrical samples of various materials and dimensions have been studied this period. One solid cylinder has been selected to calibrate the new scanning equipment. Several shell samples have been chosen from three different materials: stainless steel, aluminum, and copper. The shells also have different diameters and wall thicknesses, as listed in Table 1.

3.1.1 Solid cylinder

One stainless steel cylinder has been used to calibrate the Panametrics scanning system. The cylinder is made from machined and ground 304 stainless steel. Its dimensions are 4" diameter and 3" height. The acoustic properties of 300 series stainless at 20°C are listed in Table 2.

3.1.2 Cylindrical shells

Six cylindrical shells have been fabricated to investigate guided waves in a curved plate. The samples have been produced from commercially available thin-walled tubes. A section of 4" to 8" in length was cut from each tube and the ends machined perpendicular to the tube axis. Each sample was mounted on an acrylic disk using an RTV sealant. The RTV provides an air-tight seal around the base of the shell. The shell can be air-loaded by inverting it in the water tank, trapping air inside the shell. Table 1 lists the dimensions and materials for each of the shell specimens.

Shells 1–3 are shown in Figure 3 (left to right), and shells 4–6 are shown

Sample	Material	Diam. inches	Thickness inches
1	SS 316	6.5	.113
2	SS 301	4.5	.090
3	SS 3xx	3.5	.120
4	AL 2024	4.5	.140
5	SS 4xx	6.0	.065
6	Copper	3.125	.045

Table 1: Description of shell samples

Material	Temperature (°C)	V_l (km/s)	V_s (km/s)	ρ (g/cc)
SS 3xx	20	5.66	3.12	7.9
SS 4xx	20	6.03	3.22	7.7
Al 2024	20	6.37	3.16	2.8
Copper	20	4.70	2.26	8.9

Table 2: Acoustic properties of shell materials

in Figure 4. These figures show the relative sizes of the shell samples. Shells 1 and 3 have not been tested; the experiments have concentrated on the thin-walled shells.

The acoustic properties of the various materials are listed in Table 2. The specific steel alloy for shell 5 is unknown. However, experimental measurement of V_l has shown the shell to be 4xx series stainless steel. Shell 6 is also composed of an undetermined alloy of copper. Again, experimental measurement of V_l has confirmed the material properties. The speed of sound in water, V_f, at 20°C is 1.48 km/s. Temperature fluctuations of the water bath should be minimal. The room is temperature controlled, and the water tank contains at least 15 cu. ft. of water, providing thermal stability.
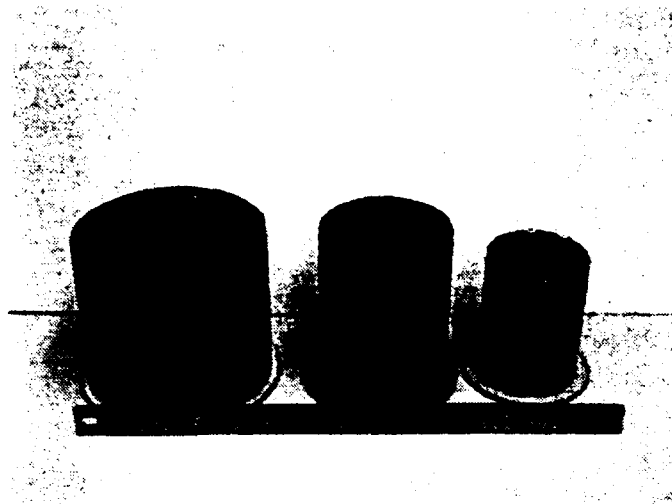
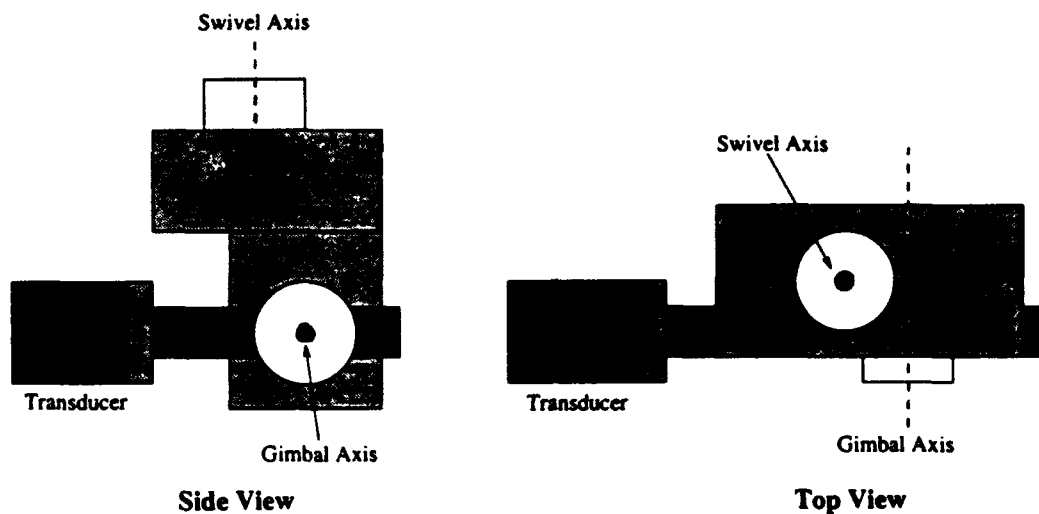Figure 3: Steel shells

Figure 4: Assorted shells

29

Figure 5: Diagram of Panametrics transducer mount

3.2 Experimental apparatus

Since the last reporting period a new scanning system and new transducers have been employed. All experiments performed during this period have used this scanning system.

3.2.1 Panametrics scanning system

The scanning system used for testing the cylindrical samples is a commercially available, multi-axis system produced by the Panametrics Co. Automated Systems Division, of Ithaca, New York. Both transducer arms have a total of five degrees of freedom. Motion of each manipulator is possible in the x, y, and z directions, as well as two rotational axes in the horizontal (swivel) and vertical (gimbal) planes. The two rotational axes are shown in Figure 5.

A full 360° of motion is available on both axes. However, the connector wire for the transducer limits the rotation to 180°. During a typical scan, the swivel angle will cover about 90°. The gimbal axis is used only in the initial calibration process.

30
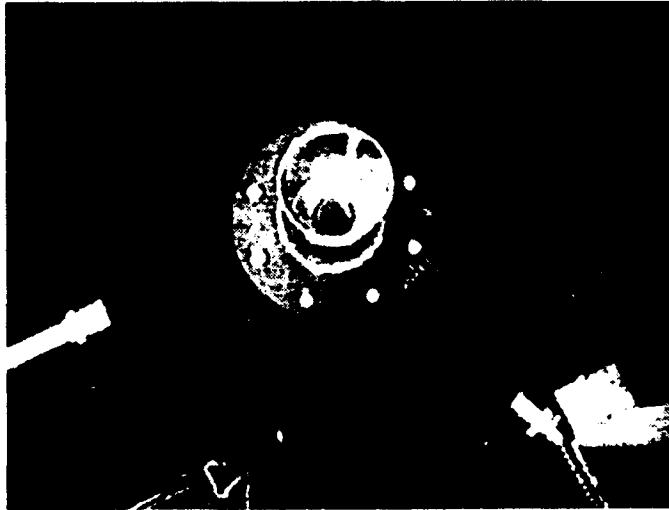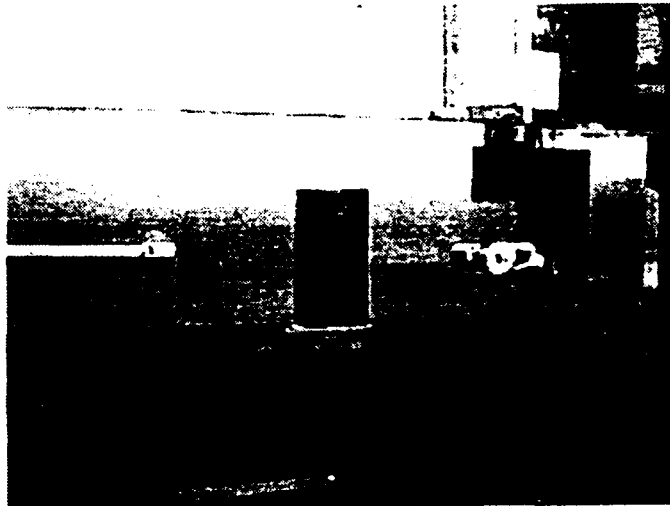
Figure 6: Top view of Panametrics scanning system

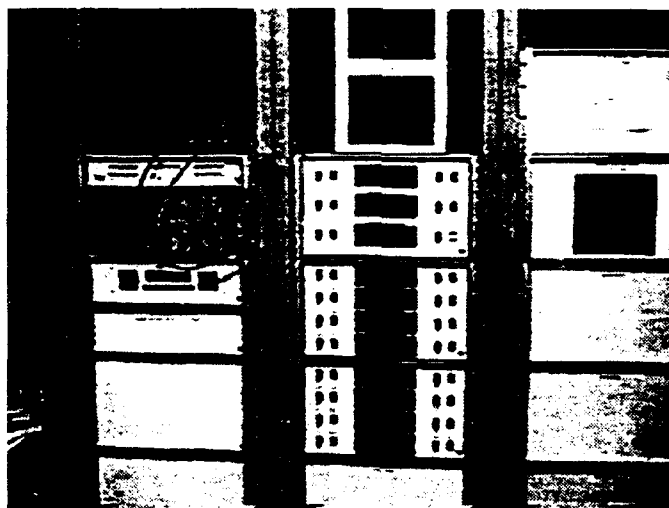Figure 7: Side view of Panametrics scanning system

31

Figure 8: Panametrics manual control panel

A top view of the water tank is shown in Figure 6 and a side view in Figure 7. In both figures, the transmitter is on the left and the receiver is on the right. A rotational stage is provided in the center of the tank for mounting the test sample. The stage is not rotated at any time during the scan. The translational arms have large motor housings on each end of the arm. The arms can approach to within 8" of each other before the housings come into contact and possibly damage the servo motors. This limits the lower bound of the observation angle. A 10" search tube is used to offset the transmitter and allow a lower observation angle. Typically, −10° is reachable by this equipment. There is no practical upper bound on the observation angle.

Two control modes are available on the system: manual and computer. Manual control is used for the initial experimental set-up and calibration of the position servos. Figure 8 is a photo of the manual control console. The left column of the console rack contains the oscilloscopes used to monitor the reflected signal. Below the top oscilloscope is the data-bus status panel. Beneath the lower oscilloscope is the control panel used for setting the machine parameters (e.g. amplifier gains, filters, excitation voltage, etc.). The center column of the rack holds the manual controls for the servo-motors.

32

Each of the eleven servos can be operated via a toggle switch on the control panel. The LED display in the center of the control panel shows the current position of each servo.

Servo positions are acquired through optical encoders on each axis of motion. The optical encoders allow for very precise positioning of the transducers, and for excellent repeatability of scans. All three translational axes have a maximum precision of 10^{-3} mm. The three rotational axes (swivel, gimbal, rotary stage) have a maximum precision of .001°. All precision values can be reset by the operator by setting a dead-band value on the computer. Typically, the dead-band for the translational axes is set to .13 mm, and the dead-band for the rotational axes is set to .01°. The high dead-band values are a result of the control system for the Panametrics system which is being developed by another group at the NDE Center. If the dead-band is set too low, the servo positioning becomes under-damped, causing the servo to oscillate between two positions.

3.2.2   Transducers

Two ULTRAN W575-1 .75" piston transducers are used as transmitter and receiver for all experiments. These transducers have a main sensitivity peak at 1MHz, but they are undamped and will also respond at 3, 5, and 7 MHz. The transmitter is generally mounted on a 5" or a 10" search tube, while the receiver is attached directly to the transducer mount. The transducers are placed at equal distances from the shell, and this distance is maintained throughout the scan.

3.2.3   Computers

A Dell 325D, 386, IBM compatible personal computer is employed for data acquisition and scanning control (Figure 9, right side). An input file containing the points in the scanning profile is generated externally and transferred to the PC. The scanning program positions the transducers at each point listed in the scan file. At each point, the transducer motion stops, and the time signal is sampled. Data are sampled at 200MHz in a window of $20\mu s$ length. The A/D converter discretizes the transducer voltage into 256 levels

Figure 9: DECstation and personal computer

(0 to 255). If the sampled time signal is clipped (i.e. the discretized voltage exceeds 255) the signal gain must be reduced manually. A test signal is sampled before each scanning run to determine the proper gain settings.

Data handling and numerical simulations are performed on a Digital DECstation 5000/240 (Figure 9, left side). Numerical analysis of the reflected field has been primarily carried out at the Polytechnic University of New York. Analysis of the experimental data is performed using software developed for this project and some commercially available software.

3.3 Testing procedure

Accurate positioning of the transducers with respect to the test specimen is required to ensure accuracy in the results. Prior to running the test scan,the transducer axis must be normal to the surface of the shell. The transducers must also be positioned 90° apart. An iterative process is used to position each of the transducers correctly.

3.3.1 Transducer position calibration

Prior to beginning a scanning session, the sending transducer must lie on the x-axis, and the receiver must lie on the y-axis. The x and y axes correspond to the two translational axes of the scanning system. Refer to Figure 10 for the calibration process of the transmitter. Prior to the calibration process, the transmitter will be at an arbitrary position (1). The transmitter is manually set to send and receive a signal pulse. A signal is reflected from the shell surface and monitored on an oscilloscope. The reflected signal is then maximized by adjusting the swivel axis. When the signal is at a maximum, the transmitter will be normal to the shell surface.

The transmitter is rotated 180° about the gimbal axis and translated along the x-axis to position (2). At this position, the swivel encoder is set to zero. Again, the reflected signal is maximized by adjusting the swivel angle (3). When the transmitter is normal to the shell, the swivel angle will have passed through 2θ degrees. Next, the swivel is rotated back θ degrees so that the transmitter is aligned parallel to the x-axis. The reflected signal is maximized a final time by translating the transmitter along the y-axis. At the location of the maximum signal, the transmitter will lie on the x-axis (4). The transmitter is moved along the x-axis to the final position (5) and rotated 180° about the gimbal axis so that it is normal to the shell surface. A similar process is employed to position the receiver on the y-axis.

When the calibration process is complete, the transducers will be in the positions shown in Figure 11. The transducers are positioned so that the distance from the shell surface to the transducer face, the water path, is 150 mm. This is an arbitrary distance. The pivot length is the distance from the swivel axis to the transducer face and is usually measured during the calibration process. Once these distances are known, the launching angle for the transmitter can be calculated using the law of cosines. The observation angle is measured counter-clockwise from the incident point of the transmitter field. Thus, a negative observation angle means that the reflected field is being sampled before the point of incidence.
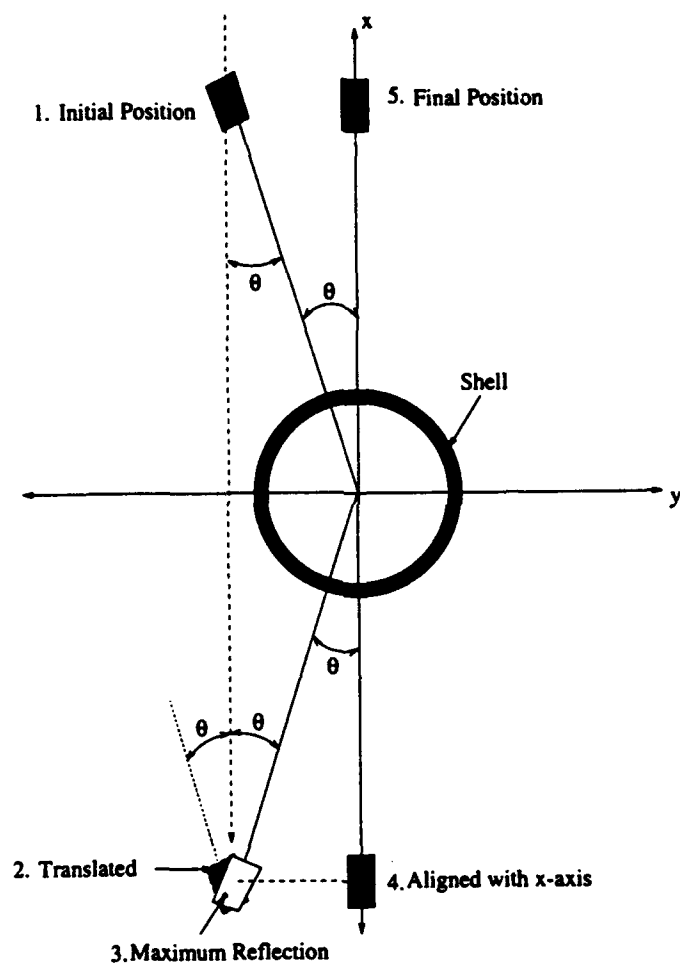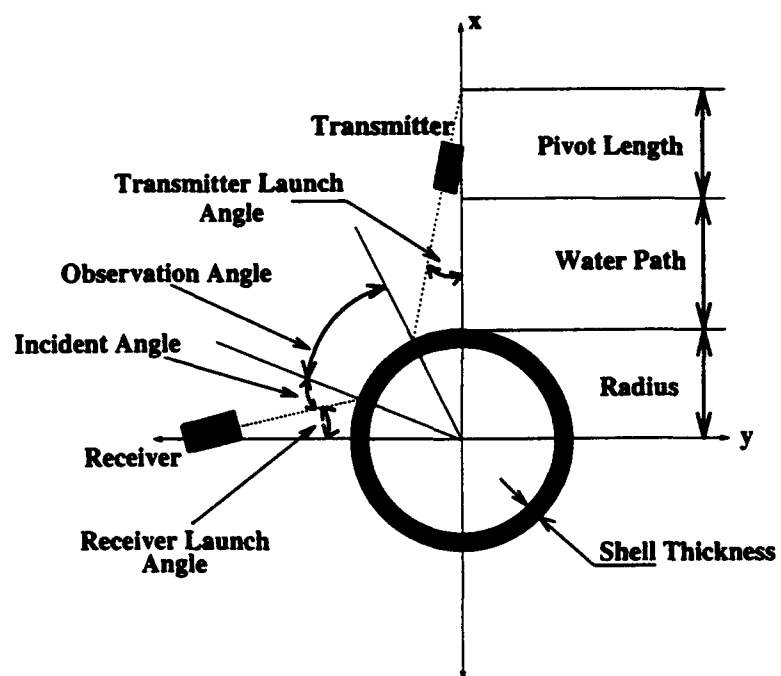
Figure 10: Calibration process

Figure 11: Initial set-up

Sample#	Material	Diameter	Thickness	Angle	
—	Steel	4"	Solid	30°	
2	Steel	4.5"	.090"	35°	39°
4	Aluminum	4.5"	.140"	13°	
5	Steel	6"	.065"	16°	33°
6	Copper	3.125"	.045"	28°	

Table 3: List of cylindrical samples

3.3.2 Data collection and manipulation

The incident angle for each shell is chosen to excite one or more guided wave modes. We assume that the curved-shell reflection coefficient poles are only slightly displaced from those of the Lamb waves, and these latter are sufficiently accurate for selecting an incident angle. A list of the incident angles for each sample is given in Table 3.

Data collection is performed by the PC and is completely automated. A total of 4000 time points are collected for each point in the scan profile. To make the data file more manageable, and to conserve storage space, the number of time points is reduced by a factor of 10. This does not affect the accuracy of the results. The data can be viewed in three forms which will be described in detail in the Results section. The first form is the raw time signal. The second form is the Fourier transformed signal, showing the full frequency spectrum. The third form is the 1 MHz band of the frequency spectrum. Most of the computations are carried out using software developed specifically for this project. ·Final visualization of the results is performed with PV-WAVE (Precision Visuals Inc.)

38

4 Results and Discussion

A series of experimental studies has been performed to evaluate the performance of the above theoretical model and to determine the feasibility of non-destructive investigation of curved structures. All of the experiments reported on below have been performed with the Panametrics system described above. Commercially available piston radiators with a frequency sensitivity peak centered at 1MHz have been used in each case. The transducers are placed 150mm from the interface being studied. Therefore, all measurements are taken in the far-field. The beam can be considered to be collimated, with the incident angle measured from the central ray of the beam.

Four steps in the analysis procedure must be performed to obtain the desired 1MHz component of the reflected field. First, the reflection coefficient poles must be located to determine the incident angle of the beam. Second, the time signals are monitored during the experiment to maintain proper gain settings. Third, the data are transformed into the frequency domain to locate and isolate the 1MHz component of the reflected field. Fourth, the 1-MHz component is displayed and compared to the theoretical model. Each step is described in detail below.

4.1 Reflection coefficient poles

Prior to running an experiment, the poles of the reflection coefficient must be located. Each pole corresponds to a guided wave in the shell wall which can be excited by an incident sound field. The incident angle of the beam is selected to excite one or more of these modes. A fluid-loaded flat plate model is sufficient to locate the poles. When the model is generalized to a curved shell, the reflection coefficient poles are displaced only slightly. The reflection coefficient of a flat plate immersed in a fluid is given by

$$R(k_1) = \frac{AS - Y^2}{(A + iY)(S - iY)} \qquad (88)$$

where

$$A = A(k_1) = (k_t^2 - 2k_1^2)^2 \tan \kappa_l h + 4k_1^2 \kappa_t \kappa_l \tan \kappa_t h,$$

39

$$S = S(k_1) = (k_t^2 - 2k_1^2)^2 \cot \kappa_l h + 4k_1^2 \kappa_t \kappa_l \cot \kappa_t h, \qquad (89)$$
$$Y = Y(k_1) = \rho k_t^4 \kappa_l / \kappa_f$$

and,

$$\rho = \rho_f / \rho_s$$
$$\kappa_{l,t,f} = \sqrt{k_{l,t,f}^2 - k_1^2} \qquad (90)$$
$$k_{l,t,f} = \omega / v_{l,t,f}.$$

The poles of the reflection coefficient are the values of the complex wave vector k_1 for which the denominator of Eq. (88) is zero. However, this function is complex and not very well behaved. To condition the function for application of a numerical search routine, the logarithm of the magnitude is used,

$$F(k_1) = \log(\,|(A + iY)(S - iY)|\, +1). \qquad (91)$$

Taking the magnitude of the function allows a minimization routine to be used to locate the poles. The logarithm tends to reduce the gradient of the function around the poles. A surface plot of Eq. (91) appears in Figure 12. The characteristic function does not have any relative minima, only absolute minima. The maxima of the characteristic function do not have any significance when taken alone; the value of the reflection coefficient numerator must also be considered.

Four propagating wave modes are visible at 1MHz: two antisymmetric modes, A_0 and A_1, and two symmetric modes, S_0 and S_1. The branch point corresponds to the critical angle for the longitudinal wave mode. A fifth pole is also visible. This is the A_2 mode, which is cutoff at 1MHz and does not propagate, owing to the large imaginary component. The numerical values for the propagating modes of the aluminum shell are listed in Table 4.

A 2-dimensional, non-gradient pattern search is used to obtain the numerical values of the poles [21]. This numerical routine can quickly locate the pole to within 10^{-5}. Since the shell is curved, the incident beam subtends a range of angles. Thus, several wave modes can be excited simultaneously, providing more information about the shell. As a greater number of poles is excited, the incident field couples more effectively with the solid interface, allowing more energy to penetrate the shell. For the aluminum shell, an
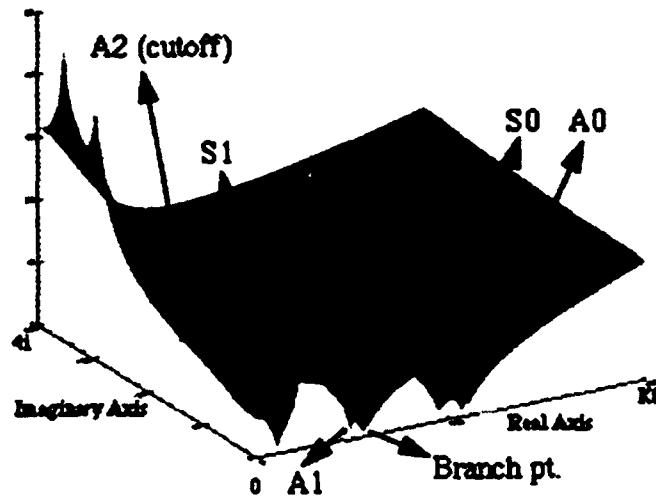
40

Figure 12: Reflection coefficient poles for Aluminum Plate

Mode	Pole location	Angle
Antisymmetric	0.9863	13.5°
·	1.1487 + 0.0405i	15.76°
	2.1804 + 0.0568i	31.04°
Symmetric	0.2896 + 0.0597i	3.90°
	0.9754 + 0.0001i	13.33°
	1.9949 + 0.0955i	28.15°

Table 4: Fluid-loaded poles for 4.5" aluminum cylinder

Mode	Pole location	Angle
Antisymmetric	$0.8623 + 0.0073i$	11.77°
	1.1101	15.22°
	$2.3288 + 0.0278i$	33.42°
Symmetric	$1.4771 + 0.0508i$	20.45°

Table 5: Fluid-loaded poles for 4.5" steel cylinder

Mode	Pole location	Angle
Antisymmetric	$0.2294 + 0.0023i$	3.11°
	1.0428	14.28°
	$2.3748 + 0.0343i$	43.17°
Symmetric	$1.2062 + 0.1875i$	16.57°

Table 6: Fluid-loaded poles for 6" steel cylinder

experiment would be conducted with the beam center incident at 30°. Both the A_0 and S_0 modes would be excited. Tables 5, 6, and 7 list the numerical values of k_1 and the incident angle in water for the propagating modes of the other samples.

Mode	Pole location	Angle
Antisymmetric	$0.2206 + 0.0030i$	2.99°
.	1.3368	18.43°
	$3.3527 + 0.0776i$	52.46°
Symmetric	$1.6190 + 0.0200i$	22.51°

Table 7: Fluid-loaded poles for 3.125" copper cylinder

4.2 Time domain analysis of the reflected field

Once the experiment has been completed, a time signal of $20\mu s$ duration has been collected for each observation angle in the scan profile. The following two figures show some sample time signals from the solid stainless steel cylinder. The angle is the observation angle measured from the tangent normal at the point of incidence. Figure 13 shows the raw time signals as sampled by the A/D converter. The discretization resolution and error are plainly visible in the time signal. The frequency spectrum shows three peaks at 1MHz, 3MHz, and 5MHz.

The discretization error and signal noise can be reduced for the weaker signals at high observation angles by increasing the signal gain. As the signal is sampled, it is averaged a minimum of ten times, suppressing most of the electronic noise. To aid in examining the time signal, a Gaussian band-pass filter, centered at 1MHz, was applied to the time signal. The resulting filtered signal is shown in Figure 14. An important feature of the time signal data is visible in this figure. As the observation angle increases, the time signal begins to separate into distinct components owing to the differing propagation times of the modes represented there. At low observation angles, the reflected signal is dominated by the specular reflection. This reflection is visible at 0° and 45°. At 60°, the signal begins to separate. The stronger component, which arrives first, is the non-specular component. The weaker component, arriving later, is the specular reflection. At 80°, the time signal becomes more highly differentiated. A weak component which arrives first is the "whispering gallery" mode (to be described in detail below). The main, non-specular or leaky wave reflection arrives second, and the specular reflection third.
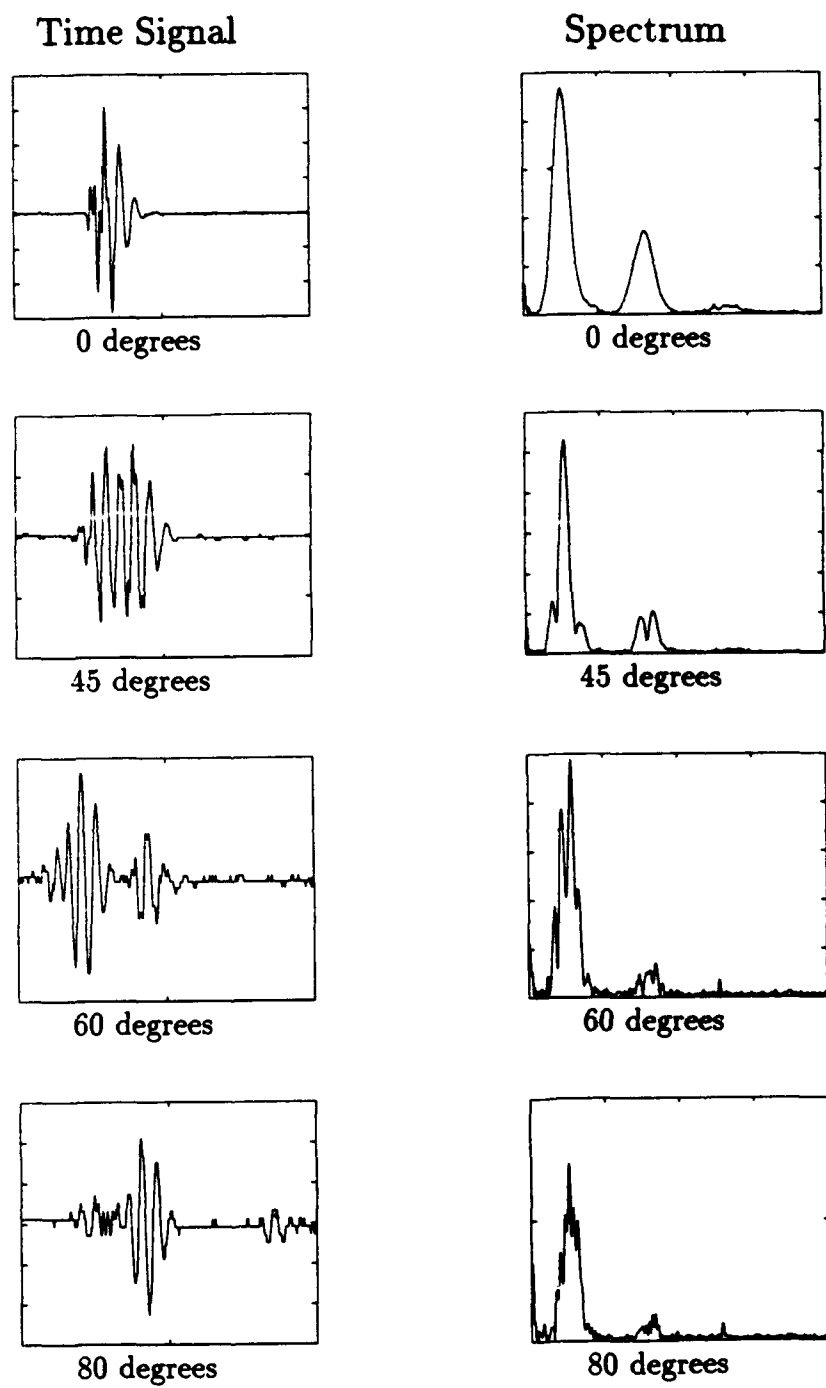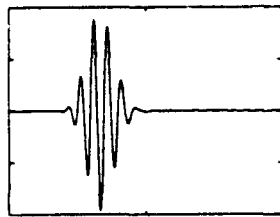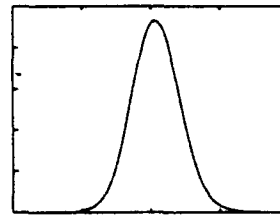
Time Signal

Spectrum

0 degrees

0 degrees

45 degrees

45 degrees

60 degrees

60 degrees

80 degrees

80 degrees

Figure 13: Unfiltered time signals

44

Time Signal

Spectrum
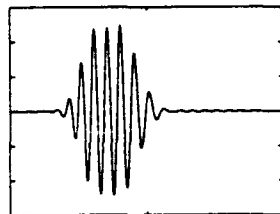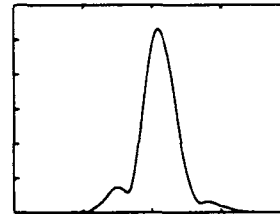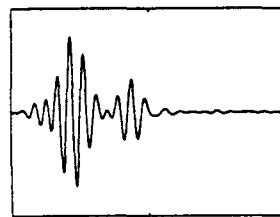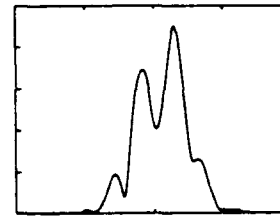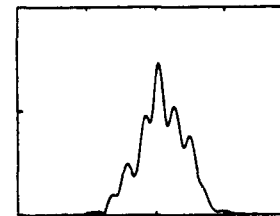

0 degrees

0 degrees

45 degrees

45 degrees

60 degrees

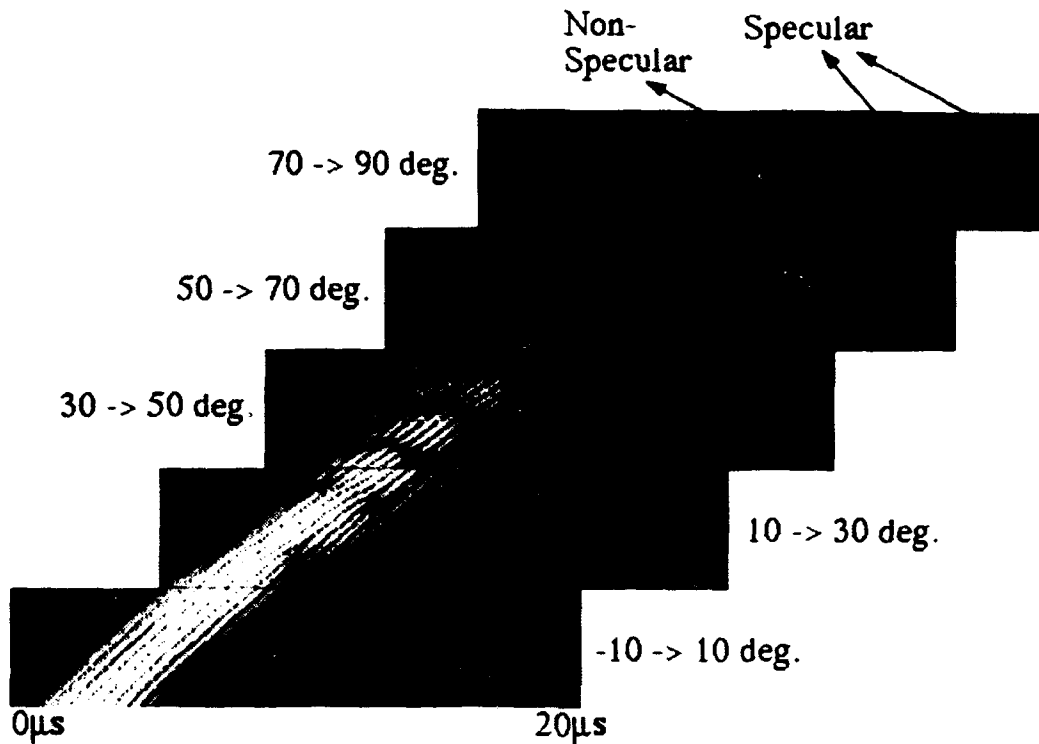60 degrees

80 degrees

80 degrees

Figure 14: Filtered time signals

Figure 15: Time signal plot for copper shell at $\theta_i = 28°$

Figure 15 shows the time signals at all angles for the air-loaded copper shell. The time signals for each observation angle are stacked vertically on the figure. The figure is divided into five bands which represent five segments of the scanning session. Because the sampling window is limited to $20\mu s$, the scanning session must be broken into segments to keep the signal within the window. The range of observation angles is listed for each segment. At low observations angles (the lower two bands), the signal is dominated by the specular reflection. Near the top of the second band, the signal begins to separate into specular and non-specular components.

Each component of the reflected signal travels a different distance and at different velocities. These paths are shown in Figure 16. The specular reflection is confined to the water. As the observation angle changes, the path the specular reflection follows changes non-linearly with respect to the
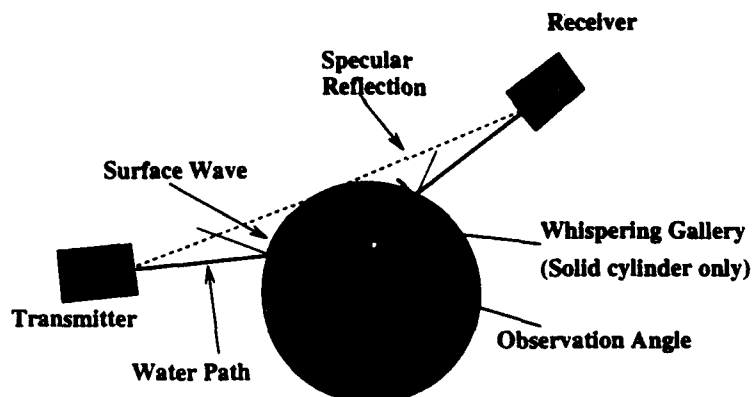
46

Figure 16: Reflected signal paths

observation angle. Thus, in Figure 15, the specular component of the signal is curved. On the other hand, the non-specular component, in this case a surface wave, travels through both the water and the fluid-solid interface. The water path is fixed during the experiment, so only the path in the shell is changing. This path changes linearly with respect to the observation angle, so the non-specular component appears linear in Figure 15. The "whispering gallery" modes are the result of the sound energy traveling at a higher velocity (transverse wavespeed) along a shorter path composed of chords along the circumference just inside the cylinder. The "whispering gallery" signal travels at V_s while the fluid signal and the surface wave travel slower, at V_f and the Rayleigh velocity, respectively. At low observation angles the "whispering gallery" signal is overwhelmed by the specular and non-specular reflections. When the signal becomes visible at higher angles, it will precede the non-specular reflection, as demonstrated above.

Each signal path has a different velocity due to the different media. The specular reflection is confined to the fluid and must travel at V_f. The non-specular component of the reflected field will travel at speed determined by the pole of the excited mode. The net result is an interference pattern due to the phase differences between the two components of the reflected field. Figure 15 clearly shows the interference between the specular and non-specular reflections. Later figures will show the interference pattern in the

47

1MHz component of the reflected field.

4.3 Frequency domain analysis of the reflected field

Of particular interest is the 1MHz component of the reflected field. To isolate the 1MHz component, the time-signal data must be transformed into the frequency domain. Figure 17 is a density plot of the reflected field for the 4.5" stainless steel shell. The vertical axis is the observation angle $-10°$ to 80°. The horizontal axis is the frequency from zero to about 8MHz. Four bands corresponding to the sensitivity peaks of the transducer are visible. From left to right, the frequency bands are 1MHz, 3MHz, 5MHz, and 7MHz. The sensitivity of the transducer is centered at 1MHz and this component of the spectrum will be used in later sections. The transducer sensitivity at higher frequencies is reduced, as demonstrated by the decreasing magnitude of the high frequency bands.

However, there is some useful information contained in this representation of the reflected field. The interference between the specular and non-specular components of the reflection is clearly visible as dark stripes passing through the frequency bands. In this view of the reflected field, the interference fringes behave as $\frac{1}{f}$. Additionally, the horizontal axis may be considered to represent fd, the frequency thickness product. By moving along the horizontal axis, keeping the frequency fixed at 1MHz, the reflected field can be examined for any given wall thickness. This has proven useful and accurate for small changes in wall thickness. Since this plot contains all of the information present in the reflected field, this representation of the field may, in fact, be more useful than the 1MHz component alone. If a defect were present in the shell, or in a layered shell, the effects of the defect on the reflected field may be more visible when looking at the entire frequency spectrum.

4.4 Reflection at a cylindrical fluid-solid interface

The following sections present the experimental results for the solid cylinder and the cylindrical shells. The experimental measurements are compared to the theoretical model when possible.

Figure 17: Angle vs. frequency density plot of reflected field from steel shell at $\theta_i = 35°$, showing the 1, 3, 5, and, 7MHz frequency bands
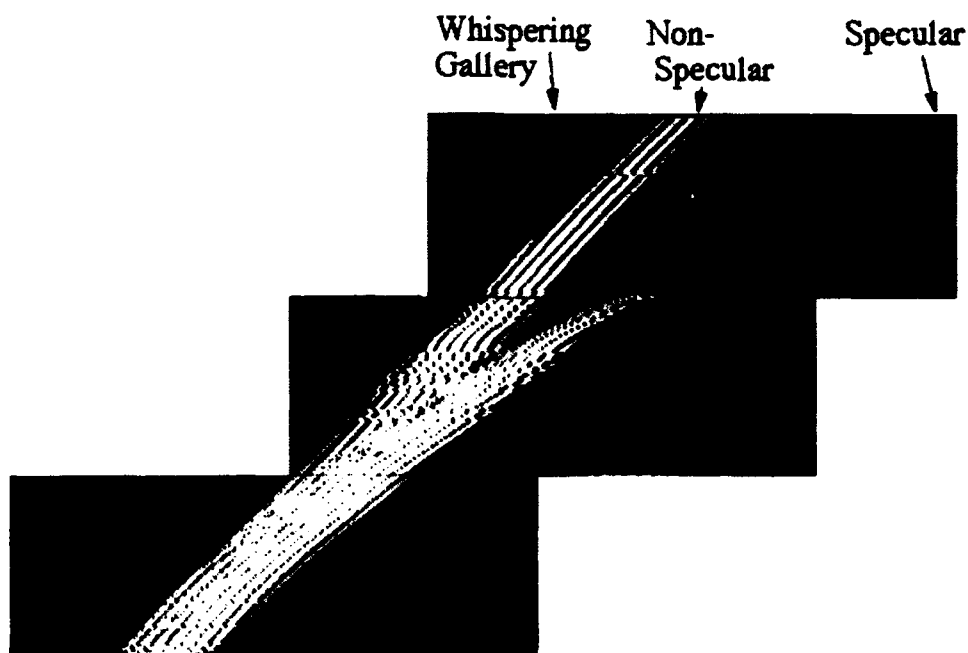
Figure 18: Time domain signal for 4.5" stainless steel cylinder at $\theta_i = 30°$

4.4.1 Reflection from a solid cylinder

Although the main focus of the research program is the cylindrical shells, a 4.5" solid stainless steel shell was examined to calibrate the new Panametrics system. For this experiment, the beam center was incident on the cylinder at 30° and the measurements wȩre all taken in the far field. The most interesting result of the experiment was the appearance of the "whispering gallery" mode. As shown in Figure 16, some of the incident energy can travel through the cylinder rather than along the surface. The "whispering gallery" signal follows the shortest path and travels at the highest velocity. Thus, in a time signal plot, the "whispering gallery" signal will arrive before the non-specular reflection. This can be seen in Figure 18.

The interference pattern characteristic of the cylindrical structures is also present, but is less visible in this case. However, if the 1MHz component of
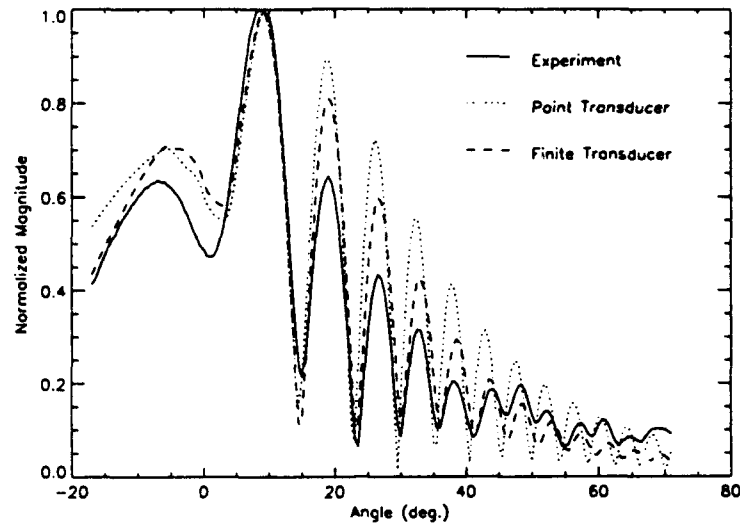
Figure 19: Reflected field from a solid 4in. stainless steel cylinder at $\theta_i =30°$

the reflected field is examined the interference pattern is much clearer. Figure 19 shows the 1MHz component of the reflected field compared to two model calculations. The reflected field and the numerical results have been normalized by their maximum values. This allows the peaks to be scaled and aligned properly. The reflected field from the cylinder is composed of three distinct regions. A monotonically increasing first mainlobe, a Gaussian-like second mainlobe which is generally greater in magnitude than the first mainlobe, and an oscillatory "trailing field." All the minima are sharply defined and accurately predicted by both theoretical models. The "trailing field" of the reflected field is lower in amplitude than predicted by both the point transducer and finite transducer models.

As the amplitude of the field decreases, the effects of the much weaker "whispering gallery" signal become visible. At an observation angle of 40°, a low spatial-frequency oscillation is superposed on the "trailing field." The superposed oscillation is at about 1/3 the frequency of the oscillations caused by the interaction of the specular and non-specular reflections. A "velocity"

51

can be inferred from the slopes of the three branches shown in Figure 18. Note that this "velocity" is not the wavespeed of the signal; it is simply a measure of the arrival time of a particular signal at the receiver for a given angle. The difference between the slopes of the "whispering gallery" branch and the non-specular branch is about one-third of the difference between the slopes of the specular and non-specular branches. This matches the low-frequency oscillation in the "trailing field."

4.4.2 Reflection from a fluid loaded cylindrical shell

A series of experimental investigations has been performed on a group of thin-walled cylindrical shells. The wall thickness of the cylinders in question range from $.75\lambda_w$ to $2.3\lambda_w$ where $\lambda_w = 1.5mm$ is the wavelength of sound in water at 1MHz. All measurements were taken in the far field, approximately 150mm from the interface. The incident angle of the sound field is measured from the beam center and the observation angle is measured counter-clockwise from the point of incidence. Any incident angle can be chosen, but to improve coupling between the incident field and the shell, the angle is chosen to coincide with one or more Lamb modes. Due to the range of angles covered by the incident field, two or more modes are often excited. The incident angles chosen for the experimental analysis are listed in Table 3 in the Procedure section above.

The non-specular reflection is a function of the shell geometry and material properties. To explore the relationship between the physical parameters and the reflected field, several different materials and configurations have been chosen. Three engineering materials have been chosen for investigation: stainless steel, aluminum, and copper. These materials provide a distribution of density, sound speed, and material damping. The geometry of the shells has been selected to examine the effects of the shell radius on the non-specular reflection. Two shells have been examined with internal fluid loading and internal air loading to determine if energy is transmitted inside the shell cavity.

As with the solid cylinder, some similar generalizations can be drawn about the reflected field from a cylindrical shell. The reflected field can be divided into three regions: a first mainlobe where the energy from the
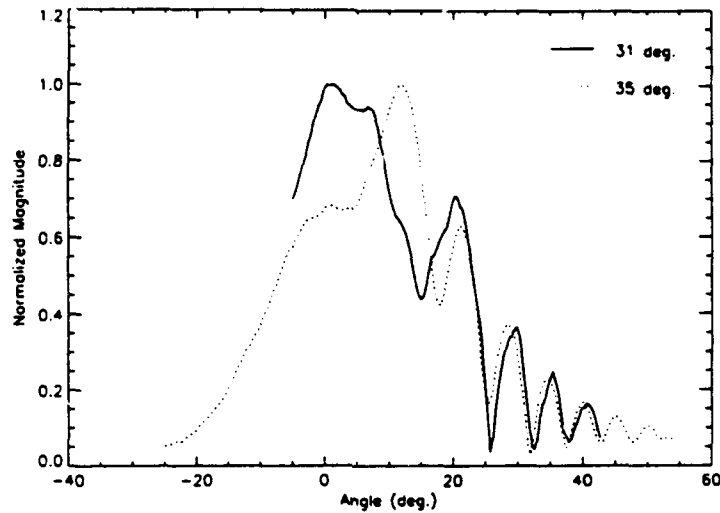
Figure 20: Comparison of reflected field for 4.5" SS shell $\theta_i = 35°, 31°$

specular reflection is concentrated, a second mainlobe where the leaky wave becomes visible, and a trailing field where the energy from the leaky wave is radiated back into the fluid. However, the relative magnitude of the first and second mainlobes depends greatly upon the experimental geometry and material properties. As expected, the first mainlobe is shifted slightly to the right of the point of incidence. For increasing angles of incidence (i.e. farther from normal incidence), the first mainlobe shifts farther to the right. This effect is demonstrated in Figure 20 for a 4-degree increment in incident angle.

The theoretical model provides excellent agreement with the experimental results. Figure 21 shows the results for an early measurement performed on the 4.5" steel shell with a 31° incident field. The oscillations in the first mainlobe are much shallower than predicted by the model. However, the model accurately predicts the oscillations and sharpness of the minima for the second mainlobe and the trailing field. The trailing field becomes lost in the ambient noise beyond an observation angle of 60°, but the oscillations are still visible. Later experiments improved the definition of the trailing field by increasing the signal gain and averaging the sampled signal.
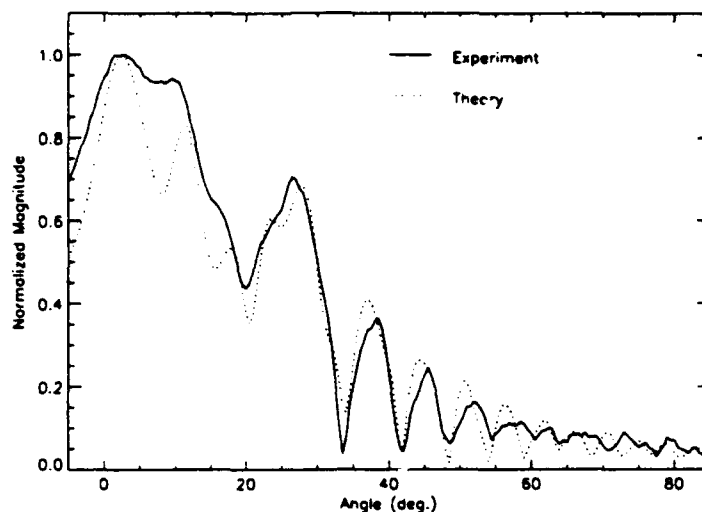
53

Figure 21: Reflected field from 4.5" SS shell at $\theta_i = 31°$

Figures 22 through 25 display the amplitude of the reflected field for the 4.5" stainless steel shell with internal fluid-loading and internal air-loading. The experimental results are compared in Figure 22 and the theoretical models are compared in Figure 23. The theoretical model predicts that the reflected field for both cases should be similar, with more damping in the fluid-loaded case. Additionally, the model predicts an oscillatory peak for observation angles prior to the point of incidence.

The measured reflected fields also match closely for positive observation angles. Higher damping is observed in the fluid-loaded shell, particularly in the trailing field. However, for observation angles below zero, the reflected fields are quite different. The reflected field from the air-loaded shell exhibits the peak predicted by the model, and agrees with the model for the entire measurement range (Figure 25).

The reflected field from the fluid-loaded steel shell does not have the predicted first peak, although agreement with the model is excellent for positive observation angles (Figure 24). For negative observation angles, the magni-
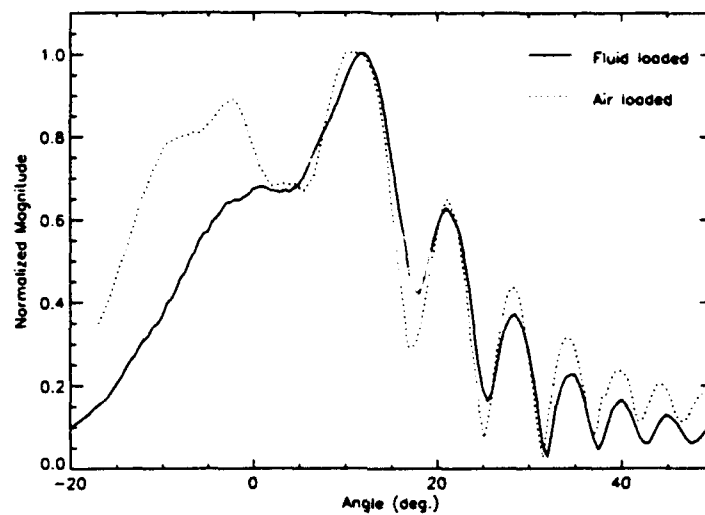
54

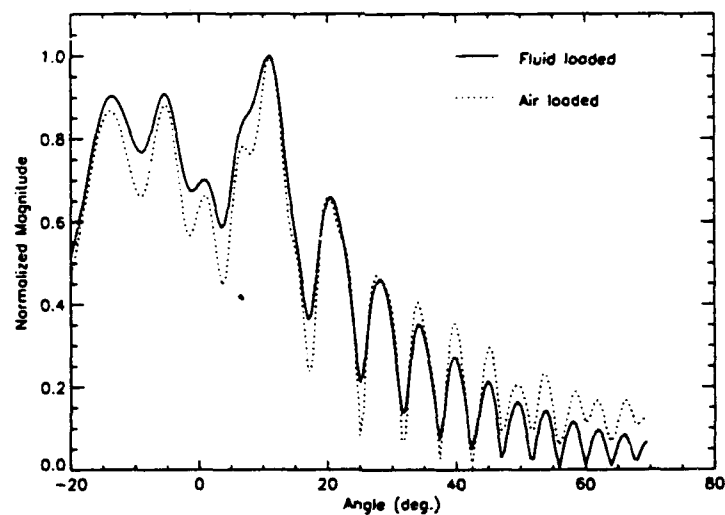Figure 22: Comparison of experimental results for 4.5" SS shell at $\theta_i = 35°$

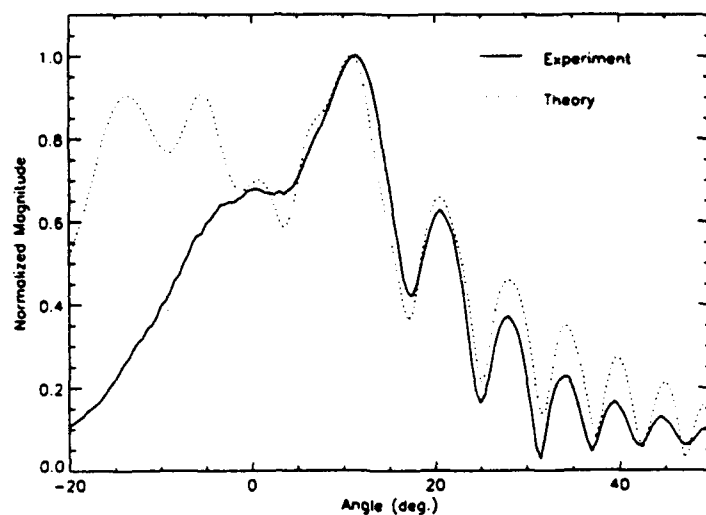Figure 23: Model comparison for 4.5" SS shell at $\theta_i = 35°$

55

Figure 24: Reflected field from fluid loaded 4.5" SS shell at $\theta_i = 35°$

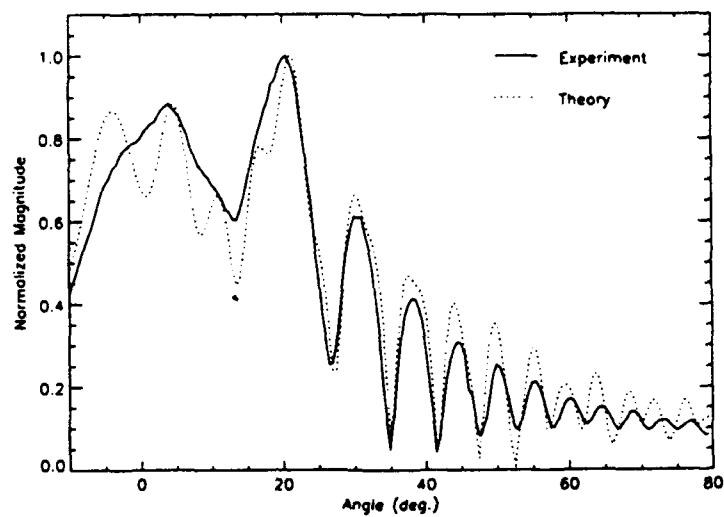
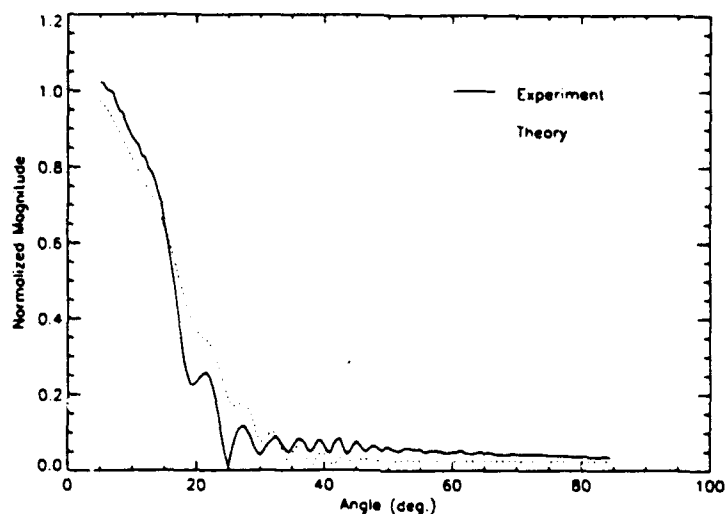Figure 25: Reflected field from air loaded 4.5" SS shell at $\theta_i = 35°$

Figure 26: Reflected field from 6" SS shell at $\theta_i = 16°$

tude of the reflected field is monotonically increasing. We believe that the first peak may be due to a signal propagating clockwise around the shell, opposite to the direction of propagation of the main sound signal. The bulk of the specular reflection will be observed counter-clockwise around the shell. Thus, this lobe of the reflected field must be caused by a plate wave propagating retrograde and radiating into the fluid. The oscillations of the peak show that there is a weak interaction between the leaky wave and the small fraction of the specular reflection that travels clockwise. The peak is well defined in the reflected field from the air-loaded shell. A greater amount of damping is present than predicted by the model, but the peak is located precisely where predicted. In the reflected field from the fluid-loaded shell, the first peak is heavily damped and appears as a plateau in the reflected field. Unlike the air-loaded shell, the fluid-loaded shell can radiate energy into the fluid from both the interior and exterior of the shell wall. Thus, the retrograde leaky wave radiates its energy more rapidly in the fluid-loaded shell.

Figure 26 presents the reflected field for the 6" diameter stainless steel
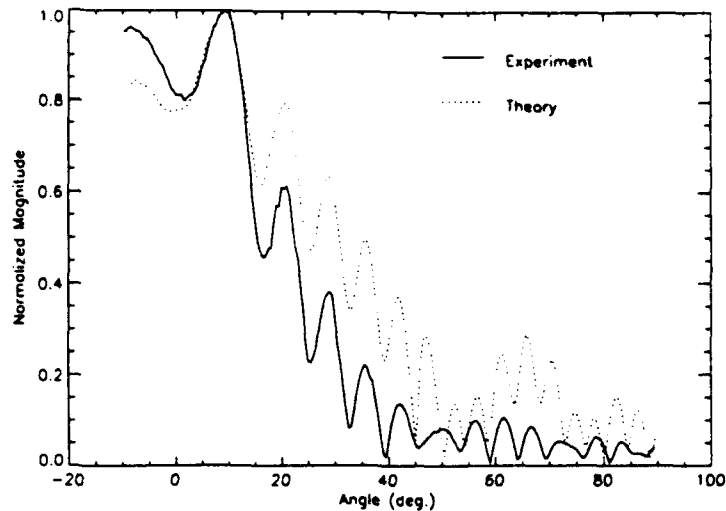
57

Figure 27: Reflected field from fluid-loaded 3.125" copper shell at $\theta_i = 28°$

shell for an incident angle of 16°. Due to the physical constraints on the Panametrics system, the smallest observation angle that could be reached was 5°. The large radius of the shell requires the plate waves to travel a greater distance for a given observation angle. Thus, when the magnitude of the reflected field is plotted against the observation angle, the field appears to attenuate rapidly.

The structure of the magnitude distribution is similar to that of the smaller 4.5" shell; the first mainlobe, second mainlobe, and trailing field are present, but deformed. Compared to the rest of the reflected field, the magnitude of the first mainlobe is greatly exaggerated. On the other hand, the second mainlobe, which usually has a comparable magnitude to the first mainlobe, is diminished in magnitude. The trailing field attenuates rapidly, disappearing at an observation angle of 50°. This behavior is accurately predicted by the theoretical model, although the minima are slightly sharper than predicted.

One copper shell was examined to explore the effect of the material prop-
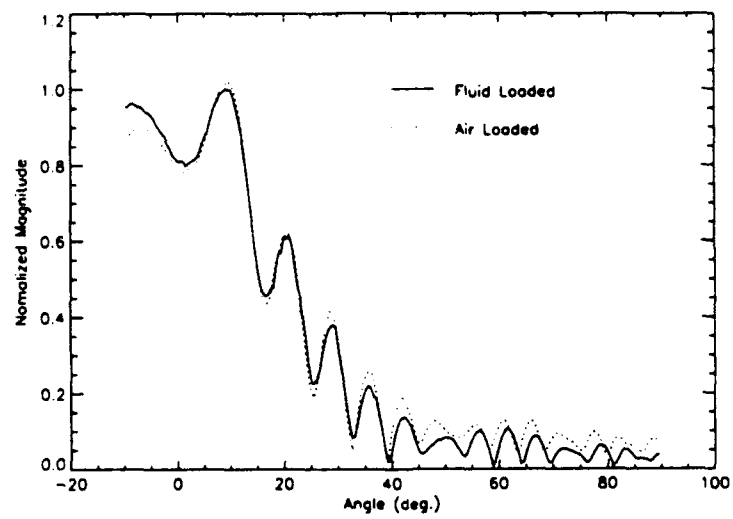
58

Figure 28: Experimental air and fluid loading comparison for copper shell, $\theta_i = 28°$

erties on the reflected field. The copper was assumed to be polycrystalline to avoid complications due to anisotropy. Measurements have proven this assumption to be valid. Copper exhibits markedly different material properties when compared to steel and aluminum. The longitudinal wavespeed in copper is about 20% less than V_l in steel and about 30% less than V_l in aluminum. The shear wavespeed, V_s, is 30% less in copper. Sound field measurements were taken using the procedures described in the above sections.

Reflected field magnitude curves for fluid-loaded and air-loaded cases are presented in Figures 27 and 28. Again, the field can be divided into three regions: a first mainlobe, slightly to the left of the point of incidence, a second mainlobe to the right of the point of incidence, and a decreasing trailing field. Currently, only the numerical model for the fluid-loaded shell is available. In this case, the numerical model does not perform as well as in the previous cases. Material damping which is present in the copper is not accounted for in the numerical model. Additional damping must be added to the model to obtain closer matching of the trailing field.

An interesting periodic effect was noted in the trailing field at 50°, 75°, and beyond. At these points, the magnitude of the peak is less than expected, giving the peak a truncated appearance. A series of identical experiments was performed to determine if the truncation was due to errors in the measurement process. However, the truncation appeared in every measurement. It was then postulated that there may be a signal traveling through the fluid inside the shell. Due to the small radius of the shell, this idea seemed plausible. The shell was tested identically to the original series, but with air filling the interior of the shell, preventing any sound from propagating inside the shell cavity. However, as can be seen in Figure 28 the reflected fields for the air and fluid loaded cases are nearly identical. The truncations appear at precisely the same locations.

Finally, the time signals from the two sets of measurements were examined and compared (Figure 15). At large observation angles, a faint signal can be seen branching off from the specular reflection to the right. The second arrow points to this signal. Since this signal appears to the right of the main specular reflection, it is either traveling at a slower velocity than the specular reflection, or traveling at the same velocity but following a longer path. This signal may be part of the specular reflection, a side-lobe from the

60

transmitter, or a signal traveling in the shell. The presence of the signal may be a result of the properties of the copper or a result of the small diameter of the shell. A measurement of the reflected field from a steel shell of equal dimensions is planned to determine the origin of this signal.

5 Summary and Conclusions

In this report we presented an extension of the two dimensional CSP model to three dimensions. The 3-D model will provide us with the capability of modeling of wave reflection from more complex 3-D objects. We have also presented the new results for cylindrical shells and have shown very good agreement between experiment and the CSP model. These experiments have provided insight into the behavior of acoustic beams at curved and planar fluid-solid interfaces. All data presented in this report were obtained using new precision experimental apparatus that is now available to us. Access to this equipment at the Center for NDE has made it possible for us to extend our measurement capabilities from CW data acquisition to time-domain pulse excitation. The new measurement scheme has provided us with a wealth of information that has lead to uncovering whispering gallery modes in solid curved structures which had not been isolated in the CW measurements.

Plans for FY 95

- Continue measurements of non-specular reflection from cylindrical shells of various materials and radii; compare results with CSP beam model prediction

- Refine model calculation and/or expe....ental procedure as necessary to accommodate real material effects

- Extend measurements and model prediction to layered shells

- Investigate the effects of visco-elasticity on experimental procedure

- Apply time-domain analysis methods to raw experimental signals

- Acquire RAM-coated samples to initiate studies on layered cylindrical shells

References

[1] D. E. Chimenti and R. W. Martin, Ultrasonics **29**, 13 (1991).

[2] V. K. Kinra and V. Dayal, Exp Mech **28**, 331 (1990).

[3] A. Schoch, "Schallreflexion, Schallbrechung and Schallbeugung", [Sound reflection, refraction, and bending], Ergeb. Exakten, Naturwiss. **23**, 127-234 (1950).

[4] H. Schmidt and F. B. Jensen, "A full wave solution for propagation in multilayered viscoelastic media with application to Gaussian beam reflection at fluid-solid interface", J. Acoust. Soc. Am., **77**, 813-825 (1985).

[5] G. V. Frisk, J. W. Dickey, and H. Überall, "Surface wave modes on elastic cylinders", J. Acoust. Soc. Am., **58**, 996-1008 (1975).

[6] H. Überall, "Surface waves in acoustics", *Physical Acoustics*, eds. W. P. Mason and R. N. Thurston, Vol. 10, (Academic Press, NY, 1973).

[7] S. Zeroug and L. B. Felsen, "Non-specular reflection of bounded beams from multilayer fluid-immersed elastic structures: complex ray method revisited", *Review of Progress in Quantitative NDE*, Vol. 11, eds D. O. Thompson and D. E. Chimenti, (Plenum, NY, 1992), 1992.

[8] S. Zeroug, "Non-specular reflection of bounded beams from multilayer fluid-immersed elastic structures", Internal report (1991), Ph.D. thesis, Polytechnic University of New York, Farmingdale, NY, (1992).

[9] J. Zhang, D. E. Chimenti, 3. Zeroug and L. B. Felsen, "Interaction of Gaussian acoustic beams with plane and cylindrical fluid-loaded elastic structures", *Review of Progress in Quantitative NDE*, eds. D. O. Thompson and D. E. Chimenti, (Plenum, NY), Vol. 11, 1992.

[10] D. E. Chimenti, J. Zhang, S. Zeroug and L. B. Felsen, "Interaction of acoustic beams with fluid-loaded elastic structures", J. Acoust. Soc. Am. **95**, 45 (1994).

[11] L. B. Felsen and N. Marcuvitz, *Radiation and Scattering of Waves* (Prentice Hall, Englewood Cliffs, N.J., 1973).

[12] G. A. Deschamps, "Gaussian beam as a bundle of complex rays," Electron. Lett., **7**, 684-685 (1971).

[13] L. B. Felsen, "Geometrical theory of diffraction, evanescent waves and complex rays", J. Roy. Astron. Soc. **79**, 77-88 (1982).

[14] S. Zeroug and L. B. Felsen, "Nonspecular reflection of two- and three-dimensional acoustic beams from fluid-immersed plane layered elastic structures", to appear in J. Acoust. Soc. Am.

[15] S. Zeroug and L. B. Felsen, "Nonspecular reflection of two- and three-dimensional acoustic beams from fluid-immersed cylindrically layered elastic structures", submitted to J. Acoust. Soc. Am.

[16] L. B. Felsen, J. M. Ho, and I. T. Lu, "Three-dimensional Green's functions for fluid-loaded thin elastic cylindrical shell: Formulation and solution", J. Acoust. Soc. Am. **87**, 546-553 (1990).

[17] L. B. Felsen, J. M. Ho, and I. T. Lu, "Three-dimensional Green's functions for fluid-loaded thin elastic cylindrical shells: Alternative representations and ray acoustic forms", J. Acoust. Soc. Am. **87**, 554-569 (1990).

[18] X. J. Gao and L. B. Felsen, "Complex ray analysis of beam transmission through two-dimensional radomes", IEEE Trans. Antennas Propagat. **AP-33**, 963-975 (1985).

[19] Y. Z. Ruan and L. B. Felsen, "Reflection and transmission of beams at a curved interface", J. Opt. Soc. Am. **3**, 566-579 (1986).

[20] A. D. Pierce, "Wave propagation on thin-walled elastic cylindrical shells", in *Elastic Wave Propagation*, eds. M. F. McCarthy and A. Hayes (Elsevier , New York, 1989) 205-210.

[21] R. Hooke and T. A. Jeeves, J. Assoc. Comp. Mach., vol 8(2), 212-229 (1961).